Zero-emission propulsion system featuring, Flettner rotors, batteries and fuel cells, for a merchant ship

Citation for the original published paper (version of record):
Arabnejad Khanouki, M., Thies, F., Yao, H. et al (2024). Zero-emission propulsion system featuring, Flettner rotors, batteries and fuel cells, for a
merchant ship. Ocean Engineering, 310. http://dx.doi.org/10.1016/j.oceaneng.2024.118618

(article starts on next page)

Ocean Engineering 310 (2024) 118618

Contents lists available at ScienceDirect

Ocean Engineering

journal homepage: www.elsevier.com/locate/oceaneng

Research paper

Zero-emission propulsion system featuring, Flettner rotors, batteries and fuel cells, for a merchant ship

Mohammad Hossein Arabnejad, Fabian Thies, Hua-Dong Yao, Jonas W. Ringsberg *

Division of Marine Technology, Department of Mechanics and Maritime Sciences, Chalmers University of Technology, 412 96, Gothenburg, Sweden

ARTICLE INFO

Keywords:
Battery
Cargo ship
Hybrid hydrogen-wind powered propulsion system
Hydrogen fuel cell
Wind power
Zero-emission

ABSTRACT

To meet the International Maritime Organization's (IMO) goal of decarbonising the shipping sector by 2050, zero-emission ship propulsion systems should be developed to replace conventional fossil fuel-based ones. In this study, we propose a zero-emission hybrid hydrogen-wind-powered propulsion system to be retrofitted to a benchmark merchant ship with a conventional propulsion system. The ship and its propulsion systems are modelled using an in-house platform. We analyse power and energy requirements for the ship over a realistic route and one-year schedule, factoring in actual sea and weather conditions. Initially, we examine the battery-powered propulsion system, which proves impractical even with a reduction in the ship's speed and the addition of a charging station. This retrofitted battery-powered propulsion system will occupy a significant portion of the existing ship's deadweight due to its substantial weight, consequently reducing the ship's cargo capacity. To address this, we evaluate integrating a hydrogen-powered fuel cell system with power equal to the non-propulsive constant load in the ship. We demonstrate that under these conditions, and with four Flettner rotors and the charging station positioned mid-port on the ship's route, the size of the zero-emission propulsion system can be approximately 20% of the deadweight, rendering such a system feasible.

1. Introduction

Shipping plays a pivotal role in the global economy, accounting for nearly 90% of worldwide trade in terms of cargo mass (Brooks and Faust, 2018). This vital sector, however, faces various environmental challenges, particularly concerning emissions. According to the International Maritime Organization (IMO) (International Maritime Organization, 2023), the shipping sector accounted for 2.89% of global anthropogenic greenhouse gas (GHG) emissions in 2018, and projections suggest a potential increase to 130% of 2008 emissions by 2050. In addition to GHG emissions, the shipping industry accounts for 12% of annual anthropogenic sulfur dioxide (SO2) emissions globally (Faber et al., 2020), with potential adverse effects on air quality and human health, particularly in port cities and coastal areas (Sofiev et al., 2018). To address these emission challenges, the IMO has established ambitious goals, setting reduction targets for GHG emissions from international shipping of at least 20% by 2030 and a minimum of 70% by 2040 compared to 2008 levels. The IMO's 2020 emissions standards also mandated a significant reduction in allowable marine fuel sulfur content from 3.5% to 0.5% by mass (International Maritime Organization, 2020).

Complying with international regulatory pressures, the marine sector is undergoing a paradigm shift towards implementing measures to lower its emissions; these measures can be broadly categorised into operational and design. Various operational measures, such as reducing vessel speed (Lindstad et al., 2011), implementing weather routing (Du et al., 2022), and optimising route planning and voyages (Wang et al., 2019), have been proposed and investigated. Despite their relatively low initial costs, these operational measures offer only a limited potential for fuel savings and a maximum GHG emissions reduction from ships of 20%. To achieve more substantial reductions and ultimately transition to zero-emission propulsion systems, design-oriented measures should be pursued, such as exploring the use of alternative energy sources (Julià et al., 2020), adopting carbon-neutral fuels (Xing et al., 2021a), and integrating hybrid propulsion systems (Damian et al., 2022). According to Xing et al. (2020), various forms of wind-assisted propulsion and hybrid power systems involving fuel cell technology offer considerable potential for reducing CO_2 emissions in the near future. Moreover, a study by Abbasov et al. (2018) suggests that a combination of zero-emission technologies, such as battery-electric and liquid hydrogen, presents viable options which are particularly advantageous as they minimise the strain on the current energy system.

The use of wind-assisted ship propulsion (WASP), particularly employing Flettner rotors, has been shown to create substantial fuel

* Corresponding author.
E-mail address: Jonas.Ringsberg@chalmers.se (J.W. Ringsberg).

https://doi.org/10.1016/j.oceaneng.2024.118618
Received 27 April 2024; Received in revised form 17 June 2024; Accepted 26 June 2024
Available online 12 July 2024

savings and environmental benefits for various types of ships. Studies by Lu and Ringsberg (2020) on Aframax Oil Tankers, Tillig and Ringsberg (2020) on tankers and RoRo cargo ships, and Ammar and Seddiek (2022) on bulk carriers reveal potential fuel savings ranging from 5.6% to 30%. Lindstad et al. (2022) further investigate the integration of WASP into a slender bulk vessel, showing that operational fuel consumption and greenhouse gas emissions can be reduced by up to 40% and 30%, respectively, with WASP accounting for two-thirds of these savings. Alkhaledi et al. (2023) evaluate the design of a liquefied hydrogen tanker ship featuring a combined-cycle gas turbine powered by hydrogen and integrated with six Flettner rotors. The study reveals that utilising Flettner rotors results in a 3.6% reduction in fuel consumption and a decrease in NOx emissions of 3.4% to 3.5%.

The integration of battery systems into ship propulsion has been shown to be a viable option to reduce emissions from the shipping sector. For short-range ferries, Gagatsi et al. (2016) show that battery-driven propulsion is both environmentally friendly and cost-effective. This aligns with the findings reported by Perčić et al. (2022) in which a fully electrified propulsion system using lithium-ion batteries for three short-sea ferries is investigated. For container ships, Kersey et al. (2022) demonstrate that purely battery-driven propulsion systems are viable if the designed routes are shorter than 1500 km. For vessels with longer routes, the integration of large-scale battery systems with hybrid propulsion appears to be a more viable option (Alnes et al., 2017). This is also evident from the study by Thies and Ringsberg (2023) which demonstrates that a purely battery-driven propulsion system could occupy more than half of the deadweight of a RoRo cargo vessel designed to travel on a 3500 km route.

The increasing production and delivery capacity of hydrogen and its declining costs have generated substantial interest in utilising fuel cells for ship propulsion systems (Han et al., 2012). However, fuel cell systems are primarily integrated with battery systems since purely fuel cell-powered systems have limited dynamic response capability to supply power for peak loads (Zhou et al., 2019). Wang et al. (2023) investigate different types of fuel cells in ship propulsion systems and conclude that low-temperature proton exchange membrane fuel cells (PEMFCs) are an optimal choice for enhanced energy efficiency, reduced carbon footprint, and cost-effectiveness. Additionally, Letafat et al. (2020) optimise the size of the hybrid propulsion system featuring a fuel cell and batteries for a ferry ship. Madsen et al. (2020) investigate a coastal research vessel equipped with a PEMFC and liquid hydrogen storage, which can achieve a 4444.8 km (2400 kn) range with significantly less GHG emissions compared to diesel-powered counterparts. Balestra and Schjølberg (2021) introduce a digital model for maritime hybrid power plants, integrating PEMFCs and batteries to design zero-emission vessels or retrofit diesel-electric ships. Xing et al. (2021b) underscore the feasibility and potential for widespread fuel cell use in naval systems and the maritime sector, provided it is enabled by technological advancements, cost reduction, regulatory support, and infrastructure development.

Despite the aforementioned advantages of wind propulsion, battery, and fuel cell systems, these technologies cannot be employed in isolation to achieve a zero-emission propulsion system for cargo vessels. For example, WASP can contribute only up to 30% of the propulsive power, and a ship equipped with this system still requires auxiliary power when anchoring at ports and manoeuvring at low speeds. Additionally, the application of purely battery-driven propulsion is limited to short-range vessels due to the low energy density and high cost of batteries (Karimi et al., 2020). Similarly, fuel cell systems are unable to provide the dynamic load required for ship propulsion systems. Consequently, a combination of these technologies is necessary to achieve a zero-emission propulsion system for merchant ships. This research investigates such a combination as a zero-emission propulsion system for a benchmark merchant ship operating in the Baltic Sea. The focus of this study is the technical and operational approaches to achieve a zero-emission solution; a cost analysis for the different alternatives is outside the scope of this study. First, using the numerical models described in the paper, the power and energy requirements are determined by simulating the ship's operation for a year on a realistic schedule based on real weather and sea data (i.e. hindcast data). With these requirements, simulations are performed for system configurations involving different battery sizes and charging scenarios, with and without Flettner rotors, and with and without fuel cell systems. The simulation results are then analysed to investigate the viability of different scenarios and propulsion systems. Finally, the propulsion systems combining fuel cell and battery technologies are optimised to reduce overall hydrogen consumption.

The remaining sections of this paper following the introduction are organised as follows: Section 2 provides an overview of the models used in the study; Section 3 then describes the studied merchant ship, its route, and schedule; Section 4 presents the results of the simulations for the ship operating for one year; finally, Section 5 presents the conclusions of the work.

2. Modelling description

In this section, we describe the modelling platform used in the paper. The platform is built in-house and is based on ShipClean (Tillig, 2020) but is implemented in Python using object-oriented programming (OOP). In this computer programming model, the software structure involves code blueprints referred to as "classes", rather than functions and logic. The classes are then employed to define individual instances, known as objects, and the program is designed around the interaction among these objects. Within the current platform, three primary classes exist: *Ship*, *ShipPerformanceSimulator*, and *Route*; a schematic representation is provided in Fig. 1. The *Ship* class defines the ship and its propulsion system. The *Route* class defines the route, including the associated weather and sea conditions. The *ShipPerformanceSimulator* includes the functionality to perform the simulation of a defined ship over a defined route. In the subsequent subsections, detailed descriptions of the classes and the implemented modelling within them are provided.

2.1. Modelling behaviour of the ship and its propulsion system

The models for the behaviour of the ship and its propulsion systems are implemented in the *Ship* class. To study different propulsion systems for the same ship, our models isolate the ship's behaviour from that of its propulsion system by implementing modules for each. For modelling the ship's behaviour, we employed the surface response modelling technique where the behaviour of the ships is quantified by finding the relationship between the response variables (i.e. variables describing the ship's behaviour) and the explanatory variables (i.e. the input parameters). Depending on the desired complexity of the modelling, there are several options for defining the ship's behaviour using the response variables. In our modelling, we assume that the response variables are drift angle, β, rudder angle, γ, required propeller thrust, T_p, and heel angle, ϕ. The input parameters for the system include the operating conditions of the ship, namely the ship speed, V_s, true wind speed, V_{wind}, true wind angle, θ_{wind}, wave height, h_{wave}, and wave angle, θ_{wave}.

To derive the response surfaces describing the ship's behaviour, we solve the steady-state equations for the balance of forces in the x and y directions (surge and sway forces) and the moments around the x and z axes (roll and yaw moments), which are expressed as:

$$\sum F_x = F_{x,\,rudder} + F_{x,\,drift} + F_{x,\,calm} + F_{x,\,wave} + F_{x,\,wind} + F_{x,\,P} + F_{x,\,FR} = 0 \quad (1)$$

$$\sum F_y = F_{y,\,rudder} + F_{y,\,drift} + F_{y,\,wind} + F_{y,\,FR} = 0 \quad (2)$$

$$\sum M_x = M_{x,\,rudder} + M_{x,\,drift} + M_{x,\,wind} + M_{x,\,FR} + M_{x,\,Righting} = 0 \quad (3)$$

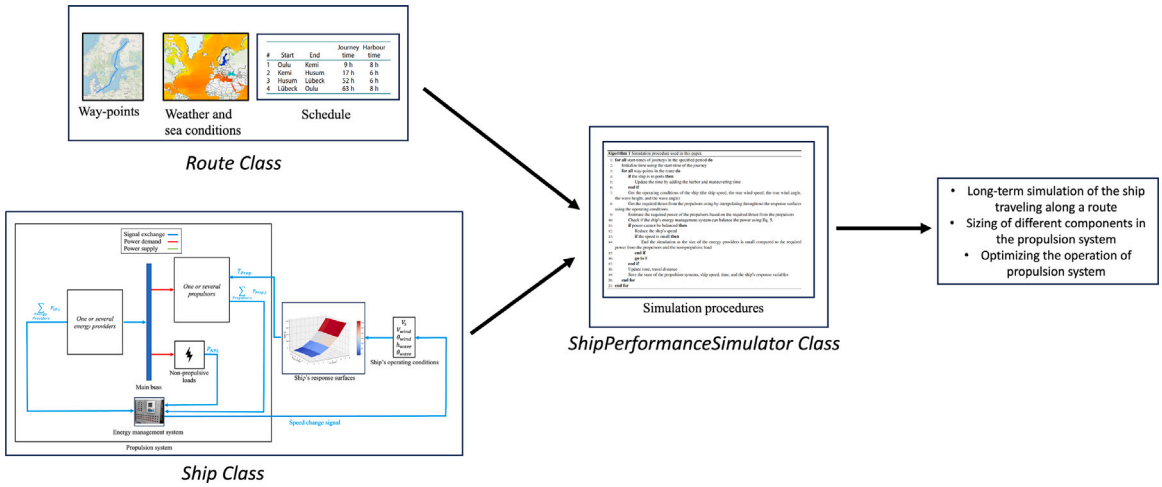

Fig. 1. Description of the platform.

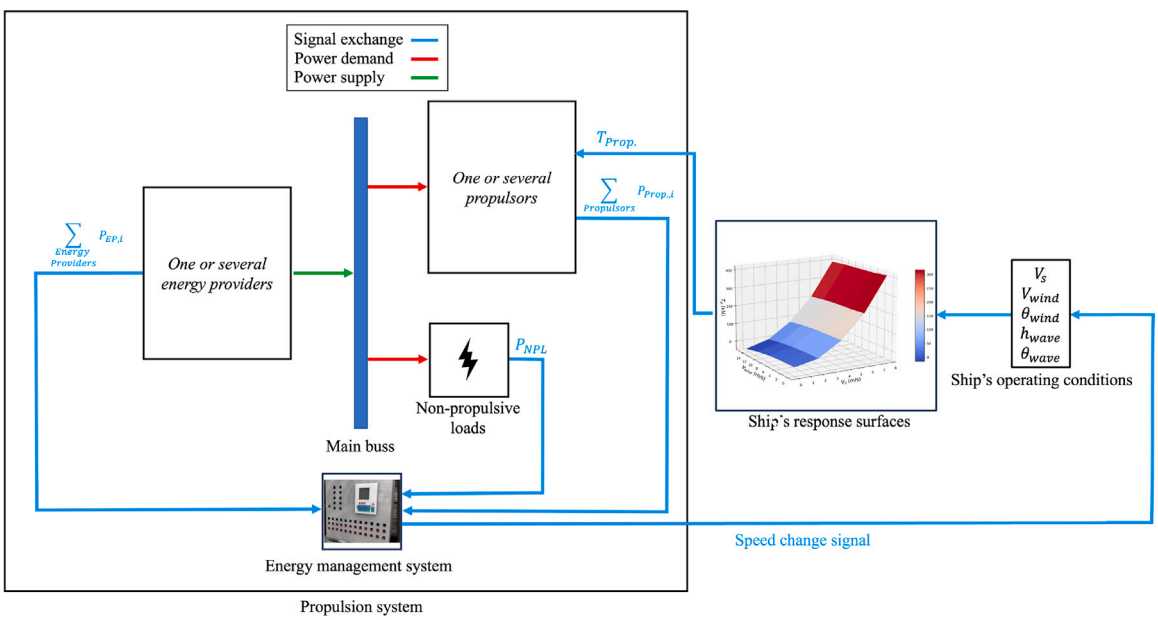

Fig. 2. The interaction between the ship propulsion systems, the response surface of the ship, and the operating conditions in the modelling used in this study.

$$\sum M_z = M_{z,\,rudder} + M_{z,\,drift} + M_{z,\,wind} + M_{z,\,FR} = 0 \tag{4}$$

where $M_{\{x,z\},\,rudder}$, $M_{\{x,z\},\,drift}$, $M_{\{x,z\},\,wind}$, $M_{\{x,z\},\,FR}$, and $M_{x,\,Righting}$ are the moments due to rudder, moments due to drift, moments due to wind, moments due to Flettner rotor system, and righting moment, respectively. These moments are obtained using the corresponding forces which are calculated as:

- The forces due to the rudder, $F_{\{x,y\},\,rudder}$, are computed using the force coefficients from Schneekluth and Bertram (1998).
- The forces due to the drift, $F_{\{x,y\},\,drift}$, are computed using the method obtained from Kramer et al. (2016).
- The calm water resistance, $F_{x,\,calm}$, is estimated from two empirical methods defined in Tillig et al. (2017).
- The added resistance in waves, $F_{x,\,wave}$, is estimated from the method proposed by Liu and Papanikolaou (2020) and ITTC (2021). It should be noted that this component of added force in waves is the most important for speed-power prediction, which is the focus of this study. The other components of the added force, which are important for predicting a ship's maneuvering performance, are not considered in this paper.
- The forces due to the presence of the Flettner rotor system, $F_{\{x,y\},\,FR}$ are obtained using the method explained in Section 2.1.3.

To model the propulsion system of the ship, we assume that it consists of one or more propulsors, one or more energy providers, and an energy management system which attempts to balance the power between the different components as:

$$\sum_{Energy\ Providers} P_{EP,i} = P_{NPL} + \sum_{Propulsors} P_{Prop.,i}, \tag{5}$$

where P_{NPL} is the non-propulsive load (hotel load), $P_{EP,i}$ is the power provided by the energy provider i, and $P_{Prop.,i}$ is the power consumed by the propulsor i. Fig. 2 depicts the interaction of the modelling of the propulsion system with the ship's response surfaces and operating conditions of the ship. At specified operating conditions, the response surfaces are utilised to estimate the required thrust for one or more propulsors in the system. Using the modelled propulsors, the required power is estimated. Subsequently, the energy management system aims to match this required power, along with the non-propulsive load, with the power provided by one or more energy providers. If the energy

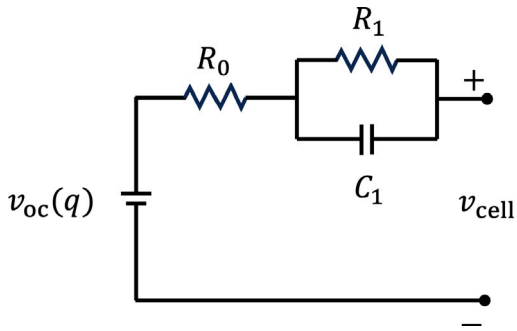

Fig. 3. Circuit model of a lithium-ion battery cell.

providers cannot supply the required power, the energy management system sends a signal to the operating conditions to reduce the ship's speed. This iterative process continues until the energy system can match the power using Eq. (5).

In the current platform used in this study, we model two energy providers—a battery system and fuel cell system—and two propulsors—a Flettner rotor system and a propeller. In the following sections, details for the modelling of all of these components are presented.

2.1.1. Battery system

In this study, the battery system is assumed to be comprised of a series of identical lithium-ion cells and a bi-directional DC-DC converter. The behaviour of the lithium-ion cells is modelled using an equivalent circuit model (ECM) (Plett, 2015). This model represents the battery with a circuit consisting of a voltage source, a resistor, and a parallel resistor-capacitor (RC) sub-circuit, all connected in series, as depicted in Fig. 3. Using this model and assuming that the cell voltage and current are constant over the time interval, Δt, the cell voltage at the interval k, $V_{cell}[k]$ can be determined using:

$$V_{cell}[k] = V_{oc,cell}(z)[k] - R_0 I_{cell}[k] + I_1[k] R_1, \tag{6}$$

where $I_{cell}[k]$ is the current passing through the cell at time $k\Delta t$, $I_1[k]$ is the current passing through the resistor R_1 at the time $k\Delta t$, and z is the state of charge. The current passing through the cell is the input to the cell while the state of charge and the current passing through the resistor R_1, $I_1[k]$, are determined from:

$$z[k+1] = z[k] - \frac{\Delta t}{Q}\eta[k] I_{cell}[k], \tag{7}$$

$$I_1[k+1] = \exp\left(-\frac{\Delta t}{R_1 C_1}\right) I_1[k] + \left(1 - \exp\left(-\frac{\Delta t}{R_1 C_1}\right)\right) I_{cell}[k], \tag{8}$$

where Q is the cell charge capacity, η is coulombic efficiency, and Δt is the time step. To use Eqs. (6)–(8) to determine the output voltage of each cell, the parameters $v_{oc,cell}$, R_0, η, Q, R_1, and C_1 are determined using experimental data provided by Zheng et al. (2016). Although these parameters can be temperature-dependent, for simplicity, we assume a constant temperature of 25 °C since we are not considering the effect of temperature on battery performance in this study. The values of $v_{OC,cell}$, η, and Q are obtained from low-current OCV tests, while R_0, R_1, and C_1 are calibrated using the differential evolution method based on the dynamic stress test (DST) test data (Fig. 4(a)). The calibrated parameters are then employed to obtain the cell voltage under a driving schedule (UDS) cycle, and the results are compared to experimental data for validation. The comparison is shown in Fig. 4(b), demonstrating good agreement between the model and experimental results.

To determine the number of cells required in the battery system, we estimate the nominal energy in the cell, denoted as E_{cell}, by fully discharging the cell at a discharge rate of 0.7 C. Discharge rate of

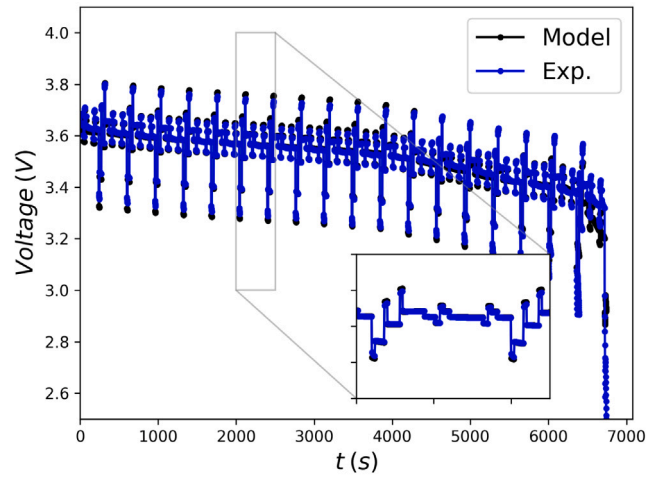

(a) Calibration

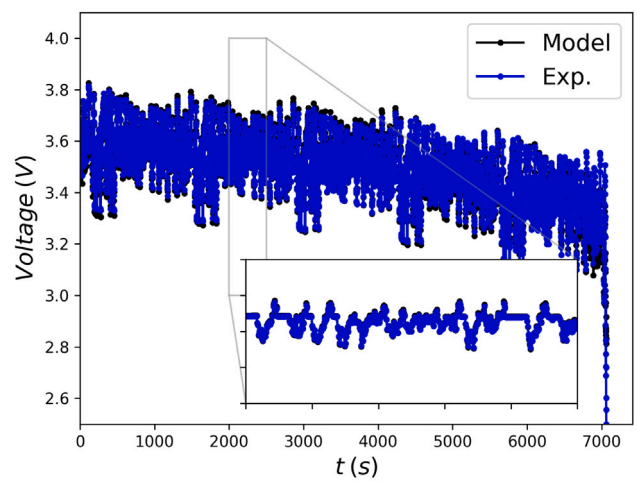

(b) Validation

Fig. 4. Calibration and validation of the ECM model for the battery cell.

1C means that the battery is discharged from fully charged to zero charge in one hour. The number of cells in the battery system can then be calculated by dividing the required energy by the nominal energy of a single cell, represented as $n_{\text{cell}} = E_{\text{batt.,req.}}/E_{\text{cell}}$. The volume and weight of the battery cell are also estimated using values for the energy density and specific energy of the Blue Whale battery system, designed by Corvus Energy (Energy, 2023). This battery system is specifically designed for marine applications and has a specific density of 0.11 kWh/kg and an energy density of 130 kWh/m^3. The power of the battery system is obtained using:

$$P_{\text{batt.}} = \begin{cases} n_{\text{cell}} P_{\text{cell}}/\eta_{\text{bc}} & \text{Charging} \\ n_{\text{cell}} P_{\text{cell}} \eta_{\text{bc}} & \text{Discharging} \end{cases} \tag{9}$$

Here, η_{bc} represents the efficiency of the bi-directional DC-DC converter, and P_{cell} is the power of a single cell. For the bi-directional DC-DC converter, we assume a constant efficiency of 0.95.

2.1.2. Fuel cell system

The power produced by the fuel cell system, P_{fcs}, is modelled by:

$$P_{\text{fcs}} = \eta_{\text{Dc/Dc, fcs}} \left(P_{\text{stack}} - P_{\text{Comp.}}\right) \tag{10}$$

where $\eta_{\text{Dc/Dc, fcs}}$ is the power efficiency of the DC-DC converter, P_{stack} is the power produced by the fuel cell stack, and $P_{\text{Comp.}}$ is the power

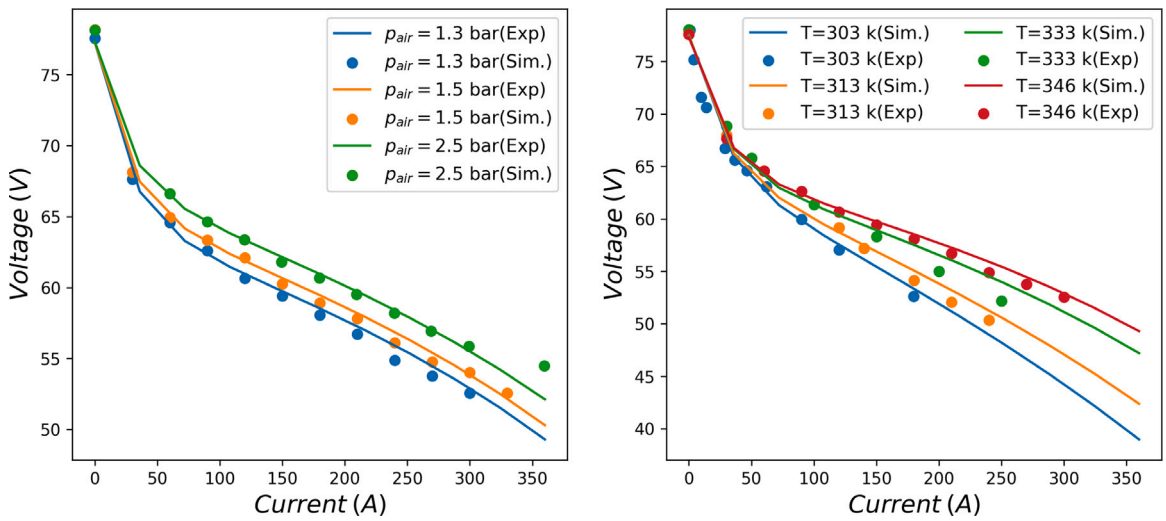

Fig. 5. Calibration of the fuel cell stack model.

consumed by the compressor. The power efficiency of the DC-DC converter is considered to be constant and equal to 0.95. The power of the fuel cell stack is obtained from:

$$P_{\text{stack}} = n_{\text{fc, cell}} P_{\text{fc, cell}}$$
$$P_{\text{fc, cell}} = v_{\text{fc,cell}} I_{\text{fc,cell}} \tag{11}$$

where $n_{\text{fc, cell}}$ is the number of the fuel cell units in the stack, and $v_{\text{fc,cell}}$, $I_{\text{fc,cell}}$, and $P_{\text{fc, cell}}$ are the output voltage of each unit, the current passing through the fuel cell stack, and the power produced by each unit, respectively. The current is the input to the system while the voltage of each unit is modelled following the method proposed by Pukrushpan (2003):

$$v_{\text{fc,cell}} = v_{\text{oc, fc}} - v_{\text{act}} - v_{\text{ohm}} - v_{\text{conc}}, \tag{12}$$

where $v_{\text{oc, fc}}$ is the open circuit voltage (OCV), v_{act} is the activation voltage loss, v_{ohm} is the ohmic voltage loss, and v_{conc} is the concentration voltage loss. The open circuit voltage can be obtained using the Nernst equation as:

$$v_{\text{oc, fc}} = 1.229 - 8.5 \times 10^{-4} \left(T_{fc} - 298.15\right) + 4.3085 \times 10^{-5} T_{fc} \left(\ln(p_{H_2}) + \frac{1}{2}\ln(p_{O_2})\right), \tag{13}$$

where T_{fc} is the temperature of the fuel cell stack, p_{H_2} is the partial pressure of hydrogen, and p_{O_2} is the partial pressure of oxygen. The activation voltage loss, v_{act}, is obtained using:

$$v_{\text{act}} = v_0 + v_a \left(1 - \exp(-a_1 i)\right),$$
$$v_0 = a_2 + a_3 \left(T_{fc} - 298.15\right) + a_4 T_{fc} \left(\ln(p_{H_2}) + \frac{1}{2}\ln(p_{O_2})\right)$$
$$v_a = \left(a_5 T_{fc} + a_6\right) \left(\frac{p_{O_2}}{0.1173} + \phi_{fc} p_{sat}(T_{fc})\right)^2 + \left(a_7 T_{fc} + a_8\right) \left(\frac{p_{O_2}}{0.1173} + \phi_{fc} p_{sat}(T_{fc})\right) + \left(a_9 T_{fc} + a_9\right) \tag{14}$$

where a_1–a_9 are the constant parameters, ϕ_{fc} is the humidity ratio of the fuel cell, and p_{sat} is water saturation pressure at the fuel cell stack temperature. The ohmic voltage loss is obtained from:

$$v_{ohm} = i R_{ohm},$$
$$R_{ohm} = \frac{t_m}{\sigma_m}$$
$$\sigma_m = b_1 \exp\left(b_2 \left(\frac{1}{303} - \frac{1}{T_{fc}}\right)\right) \tag{15}$$

where b_1 and b_2 are constant parameters and t_m is the membrane thickness. The concentration voltage loss can be obtained from:

$$v_{\text{conc}} = i \left(c_1 \frac{i}{i_{max}}\right)^{c_2}$$
$$c_1 = \begin{cases} \left(c_3 T_{fc} + c_4\right)\left(\frac{p_{O_2}}{0.1173} + \phi_{fc} p_{sat}\right) + \left(c_5 T_{fc} + c_6\right) \frac{p_{O_2}}{0.1173} + \phi_{fc} p_{sat} < 2 \text{ atm} \\ \left(c_7 T_{fc} + c_8\right)\left(\frac{p_{O_2}}{0.1173} + \phi_{fc} p_{sat}\right) + \left(c_9 T_{fc} + c_{10}\right) \frac{p_{O_2}}{0.1173} + \phi_{fc} p_{sat} \geq 2 \text{ atm} \end{cases} \tag{16}$$

where c_2-c_{10} are the constant parameters. In the above equations, several parameters need to be adjusted to achieve the correct behaviour of the fuel cell stack under different operating conditions. We performed parameter tuning to closely match the experimental data from Corbo et al. (2007) using the least mean square algorithm. The determined constant parameters are presented in Table 1. The fuel cell stack consists of 80 fuel cell units and was tested under varying air pressure and fuel cell stack temperatures. The fuel cell stack has a capacity of 20 kW. Fig. 5 compares the polarisation curve obtained from the calibrated model with the experimental data under different operational conditions. As can be seen from the comparison, the calibrated model accurately captures the behaviour of the fuel cell.

The power required by the compressor, $P_{\text{comp.}}$, can be estimated using:

$$P_{\text{comp.}} = \frac{c_{p,\text{air}}}{\omega_{\text{comp.}}} \frac{T_{\text{amb.}}}{\eta_{\text{comp.}}} \left(\left(\frac{p_{\text{comp., out}}}{p_{\text{amb.}}}\right)^{(\gamma-1)/\gamma} - 1\right) \dot{m}_{\text{air}} \tag{17}$$

where $c_{p,\text{air}}$ denotes the specific heat capacity of air at constant pressure, $\omega_{\text{comp.}}$ represents the rotational speed of the compressor, $\eta_{\text{comp.}}$ is the isentropic efficiency of the compressor, $\dot{m}_{\text{air}}$ is the mass flow rate of air passing through the compressor, $p_{\text{comp., out}}$ is the pressure at the compressor outlet, γ stands for the heat capacity ratio, and $p_{\text{amb.}}$ and $T_{\text{amb.}}$ are the ambient pressure and temperature, respectively. The mass flow rate of air is calculated based on the oxygen mass flow rate required for the fuel cell stack to generate the specified power. The isentropic efficiency and rotational speed of the compressor are obtained from its performance map, which is based on the model proposed by Casey and Robinson (2013). The constants in this model are calibrated using the least mean square method, utilising experimental data presented in Wan et al. (2017), in which the authors conducted an experimental study on a centrifugal compressor designed for a 65 kW fuel cell system. Fig. 6 presents a comparison between the pressure ratio and efficiency as a function of air mass flow rate at various

Table 1
Constant parameters in Eqs. (14), (15), and (16).

Parameter	Value	Parameter	Value	Parameter	Value
a_1	$2.59998790 \times 10^{-1}$	a_9	$4.89999380 \times 10^{-1}$	c_7	$1.68040546 \times 10^{-4}$
a_2	$-7.92072947 \times 10^{-4}$	b_1	$6.35473188 \times 10^{-2}$	c_8	$-6.79997851 \times 10^{-2}$
a_3	$4.07592080 \times 10^{-5}$	b_2	1.5×10^{3}	c_9	$-5.08414071 \times 10^{-5}$
a_4	$-1.74329138 \times 10^{-5}$	c_2	2.49999996	c_{10}	$4.00000281 \times 10^{-1}$
a_5	$1.64989025 \times 10^{-2}$	c_3	$7.08059458 \times 10^{-4}$		
a_6	$2.49915211 \times 10^{-4}$	c_4	$-6.22000304 \times 10^{-1}$		
a_7	$1.66000398 \times 10^{-1}$	c_5	$-1.50750353 \times 10^{-3}$		
a_8	$-6.31104623 \times 10^{-4}$	c_6	1.67999975		

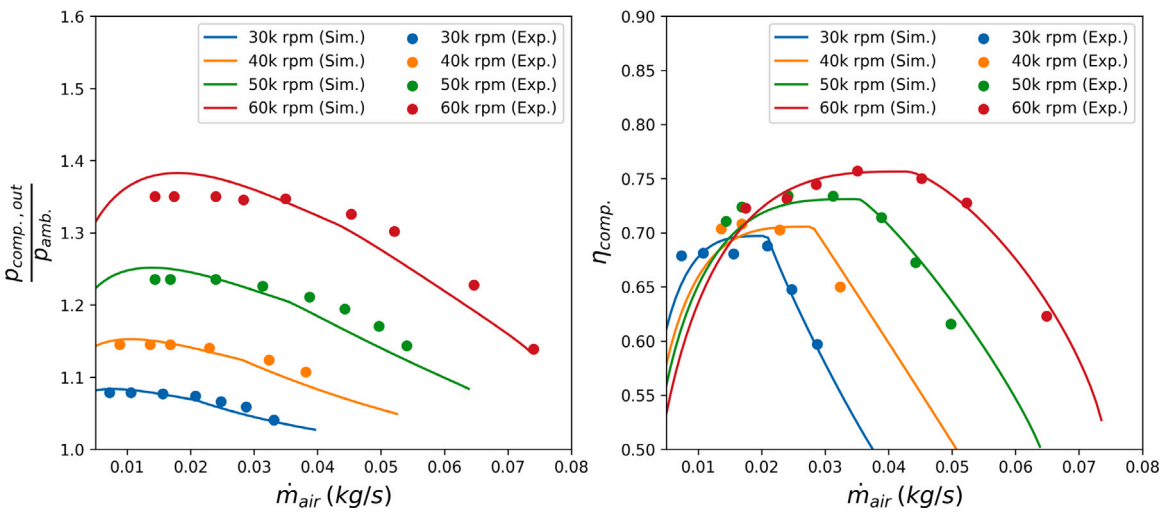

Fig. 6. Comparison between the calibrated compressor model and the experimental data from Wan et al. (2017).

tested rotational speeds, for predicted and experimental values. The results demonstrate that the calibrated model effectively represents the compressor's behaviour.

To determine the required size of the hydrogen tank, the mass flow rate of the consumed hydrogen, $\dot{m}_{H_2,\ stack}$, is calculated from:

$$\dot{m}_{H_2,\ stack} = \frac{I_{fc,cell} n_{fc,\ cell} M_{H_2}}{2F}, \tag{18}$$

where M_{H2} represents the molar mass of hydrogen and F is the Faraday number. To estimate the volume of the hydrogen tanks, we consider two storage technologies: liquid hydrogen (LH2) and Cryo-compressed hydrogen (CcH2). These technologies are considered the most feasible methods for storing hydrogen in large ships, as indicated in the review paper by Wang et al. (2021). LH2 technology involves storing hydrogen at temperatures around 20 K and pressures around 1 bar, while CcH2 technology involves hydrogen storage temperatures and pressures of approximately 35 K and 250 bar, respectively. The hydrogen density under these conditions is denoted as $\rho_{LH2} = 71$ kg/m^3 and $\rho_{CcH2} = 80$ kg/m^3. These density values are then used to determine the required volume of the hydrogen tank.

To determine the size of the fuel cell system based on the required power, the number of the fuel cell units is initially estimated by assuming that the required power from the compressor is zero. Using this assumption and the maximum power of each fuel cell unit, the number of the cell units, $n_{fc,\ cell}$ is determined from Eq. (11). Subsequently, the required air mass flow rate at the maximum power of the fuel cell stack, $\dot{m}_{air,\ stack,\ max}$, can be obtained from:

$$\dot{m}_{air,\ stack,\ max} = \frac{\lambda_{O_2} I_{fc,cell,max} n_{fc,\ cell} M_{O_2}}{4 \chi_{O_2} F}. \tag{19}$$

where $I_{fc,cell,max}$ is the maximum current of the fuel cell stack, M_{O_2} is the molar mass of the oxygen, λ_{O_2} is the stoichiometric ratio of oxygen which is assumed to be 2, and χ_{O_2} is the mass fraction of oxygen in air. Using this air mass flow rate and with the assumption that the flow coefficient, $\phi_{comp.}$, and the work coefficient, $\psi_{comp.}$, should be kept constant during the scaling of the compressor, the scaling factor for the compressor, $\alpha_{comp.}$, and the rational speed of the compressor at the design condition, $\omega_{comp.,des.}$, can be determined using:

$$\alpha_{comp.} = \frac{\dot{m}_{air,\ stack,\ rated}}{\dot{m}_{base,\ des.}},\ \omega_{comp.,des.} = \frac{\omega_{base,\ des.}}{\sqrt{\alpha_{comp.}}} \tag{20}$$

where $\dot{m}_{base}$ and $\omega_{base,\ des.}$ represent the mass flow rate of air and the rotational speed of the base compressor at the design condition, respectively. The base compressor considered in this study is a centrifugal compressor designed by Wan et al. (2017) for a 65 kW fuel cell system. This compressor is used to calibrate the compressor model, as mentioned previously. By considering the power used by the compressor and the maximum power produced by the fuel cell stack, we can then calculate the maximum net power of the fuel cell system using Eq. (10). This power is slightly lower than the maximum power required for the system, since we initially assumed that the demand power from the compressor is zero. The number of fuel cell units and the scale factor of the compressor are then iteratively adjusted so that the maximum power produced by the fuel cell system matches the maximum required power from the system. To estimate the weight and volume of the fuel cell system, we linearly scale the weight and volume of Ballard's 200 kW fuel cell system, FCwave, which is specifically designed for marine applications. This system weighs 1000 kg and has a volume of 1.97 m^3.

2.1.3. Flettner rotor system

The power consumed by the Flettner rotor system is calculated as the sum of the power consumed by the Flettner rotor(s) in the system

as:

$$P_{frs} = \sum_{n=1}^{n_{fr}} P_{fr} \tag{21}$$

where n_{fr} is the number of rotors and P_{fr} is the power consumed by each rotor, which is determined by:

$$P_{fr} = \frac{1}{2}\rho_{air} A_{FR} V_{wind}^3 C_{p,FR} \tag{22}$$

where ρ_{air} is the air density, A_{FR} is the projected area of the Flettner rotor, and V_{wind} is apparent wind speed. $C_{P,FR}$ is the power coefficient in each rotor which is determined by:

$$C_{P,FR} = 10^{-4} SR^5 - 4\cdot 10^{-4} SR^4 + 0.0143 SR^3 - 0.0168 SR^2 + 0.0234 SR \tag{23}$$

where SR is the spin ratio defined as:

$$SR = \frac{\omega_{FR} d_{FR}}{2V_{wind}} \tag{24}$$

where ω_{FR} is the rotational speed of the rotor in rad/s and d_{FR} is the diameter of the rotor.

The thrust, $F_{x,FR}$, the side force, $F_{y,FR}$, and the moments due to the rotor are determined by projecting the lift, L_{FR}, and drag, D_{FR}, forces on the coordinate system used in Eq. (4). These forces are obtained by:

$$L = \frac{1}{2} A_{FR} \rho_{air} V_{wind}^2 C_{l,FR} \tag{25}$$

$$D = \frac{1}{2} A_{FR} \rho_{air} V_{wind}^2 C_{d,FR}, \tag{26}$$

where $C_{d,FR}$ and $C_{l,FR}$ are the drag and lift coefficients, respectively. These coefficients are obtained from:

$$C_{l,FR} = \begin{cases} 0.02145\, SR^5 - 0.1824\, SR^4 \\ \quad + 0.05744\, SR^3 + 1.622\, SR^2 + 0.6832\, SR & SR \le 3.4 \\ 8.5 & SR > 3.4 \end{cases}$$

$$C_{d,FR} = \begin{cases} \begin{cases} C_{d,Ref.} & \frac{C_{l,Ref.}}{C_{d,Ref.}} < 0.001 \; or \; SR < 0.1 \\ \frac{C_{d,Ref.} C_{l,FR}}{C_{l,Ref.}} & else \end{cases} & SR \le 3.4 \\ 3.0 & SR > 3.4 \end{cases} \tag{27}$$

$$C_{l,FR} = \max(C_{l,FR}, 0)$$

$$C_{d,FR} = \max(C_{d,FR}, 0.4)$$

where $C_{d,Ref.}$ and $C_{l,Ref.}$ are the reference lift and drag coefficients given by:

$$\begin{aligned} C_{l,Ref.} &= -0.0046\, SR^5 + 0.1145\, SR^4 - 0.9817\, SR^3 \\ &\quad + 3.1309\, SR^2 - 0.1039\, SR \\ C_{d,Ref.} &= -0.0017\, SR^5 + 0.0464\, SR^4 - 0.4424\, SR^3 + 1.7243\, SR^2 \\ &\quad - 1.641\, SR + 0.6375 \end{aligned} \tag{28}$$

Eq. (23) and Eqs. (27) and (28) are based on the results in Li et al. (2012), but they have been slightly modified to match the full-scale measurements. For details of this modification, the reader can refer to Tillig and Ringsberg (2020).

The aerodynamic interaction between the Flettner rotor is considered following the method proposed by Tillig and Ringsberg (2020). The spin ratio, SR, is optimised to maximise the power saving by using the Flettner rotor system for each operating condition of the ship.

2.1.4. Propeller

The shaft power consumed by the propeller, P_p, is obtained from:

$$P_p = \frac{P_E}{\eta_R \eta_o \eta_S \frac{1-t}{1-w}} \tag{29}$$

where P_E is the required effective power, η_R is the relative-rotative efficiency, η_o is the open water efficiency, η_S is the shafting efficiency, t is the thrust deduction factor, and w is the wake fraction. The required effective power is calculated from:

$$P_E = T_p V_s \tag{30}$$

where T_p is the propeller thrust and V_s is the ship's speed. In this work, the wake fraction is estimated based on the approximation presented in Kristensen and Lützen (2012) and Harvald (1992). The thrust deduction factor is calculated by assuming that the hull efficiency is between 1.05 and 1.1, based on the relation proposed by Schneekluth and Bertram (1998). The relative rotative efficiency is also obtained using the method presented by Holtrop and Mennen (1982), and the shafting efficiency is assumed to be 0.99. The open water efficiency is calculated based on the thrust coefficient, K_T, and the torque coefficient, K_Q, which are obtained using the polynomial presented in Oosterveld and van Oossanen (1975).

2.2. Defining the route and ship's operating conditions

Defining the route and the weather and sea conditions is implemented in the *Route* class. The ship's route is defined based on information about its legs and their voyage time, the harbour times at each port, the manoeuvre time at the ports, and the names of the ports where a charging facility is available, along with the available charging power. The route also includes a schedule, which can be weekly or daily. Each leg is defined using the names of the origin and destination port and the geographical locations (longitude and latitude) of way-points. Using the voyage times for each leg and the manoeuvre time at the origin and the destination of each port of the leg, the average speed of the ship at each leg is calculated. The weather and sea conditions at each way-point are also obtained from the Copernicus Marine Environment Monitoring Service (CMEMS) using the geographical locations of the way-points. These conditions include wind speeds and directions, as well as wave heights and directions. These weather and sea conditions, along with the estimated average ship speed, are assumed to be the same as the operating conditions at the way-points, as shown in Fig. 2.

2.3. Simulation procedure

All functionality related to the simulation procedure of a ship travelling on a route is implemented in the *ShipPerformanceSimulator* class. Algorithm 1 presents the procedure implemented in this class for simulating the ship's travel over a specific route during a predefined period based on a set schedule. The algorithm iterates over all start times of the voyages within the specified period and iterates over all the way-points in the route, updating the time using harbour and manoeuvring times if the ship is at a port. The algorithm further utilises the location of the way-point and the time to obtain information on weather and sea conditions. Using the weather and sea conditions, along with the ship speed at the way-point, the required thrust from the propulsors is calculated using the ship's response surface. Subsequently, the required thrust values are used to determine the required power for all propulsors. The energy management system then attempts to balance this power with the power supplied by the energy providers. If this balance is achieved, the algorithm updates the time, the travelled distance, the states of the propulsors, and the energy systems, then saves the data and moves to the next way-point. If this balance cannot be achieved, indicating that the energy providers are unable to supply the required power for the propulsors, the algorithm reduces the ship's speed and the energy management process continues to match the power between the energy providers and the propulsors; this trial-and-error process persists until a match is found. If the energy management system cannot establish a balance even after reducing the speed to a minimal value, the algorithm terminates the voyage. When this occurs, it is assumed that the voyage must be cancelled due to insufficient power from the energy providers to complete the voyage.

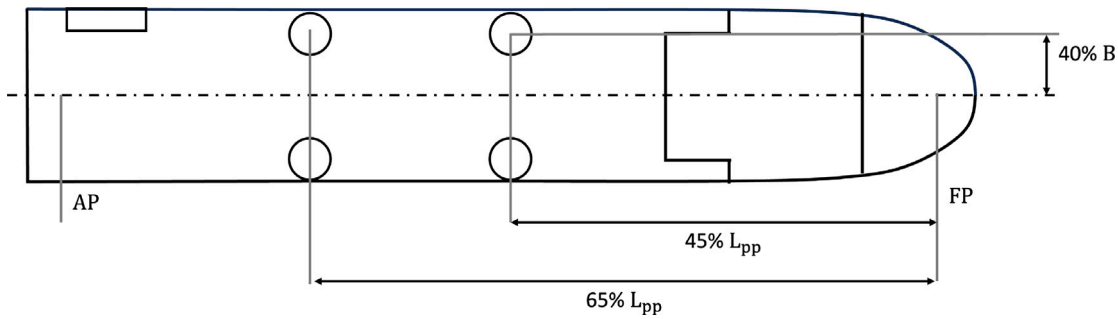

Fig. 7. Location of Flettner rotors in respect to the AP and FP of the ship (L_{pp} is the length between the AP and FP; B is the beam length).

Table 2
Specifications of the Tavastland RoRo cargo vessel.

Length overall	190.8 m
Beam	26.44 m
Draft, full load	7.8 m
Deadweight	15960 t
Displacement	24050 t
Fuel oil capacity	1260 t
Design speed	15.10 kn
Total lane meters	2774 m
Installed propulsive power	19 MW
Installed auxiliary power	3 MW

Algorithm 1 Simulation procedure used in this study.

for all start-times of voyages in the specified period **do**
  Initialise time using the start-time of the voyage
  for all way-points in the route **do**
    if the ship is in ports **then**
      Update the time by adding the harbour and manoeuvring time
    end if
    Get the operating conditions of the ship (the ship speed, the true wind speed, the true wind angle, the wave height, and the wave angle)
    Get the required thrust from the propulsors by interpolating throughout the response surfaces using the operating conditions
    Estimate the required power of the propulsors based on the required thrust from the propulsors
    Check if the ship's energy management system can balance the power using Eq. (5).
    if power cannot be balanced **then**
      Reduce the ship's speed
      if the speed is small **then**
        End the simulation as the size of the energy providers is small compared to the required energy from the propulsors and the non-propulsive load
      end if
      go to 8
    end if
    Update time, travelled distance, and the states of propulsors and energy providers
    Save the results
  end for
end for

3. Study case

The ship examined in this study is a RoRo cargo vessel named Tavastland, which operates in the Baltic Sea. Table 2 lists the ship's specifications. The vessel features a large free deck, approximately 86 meters in length. Traditionally, this deck space accommodates dedicated lanes for cars and trucks. However, with the proper installation of foundations and roofing, this area has the potential to be repurposed for the integration of Flettner rotors. In this study, we considered two ship configurations: one equipped with four Flettner rotors and one without. Throughout the study, we refer to the former as the ship with WASP and the latter as the ship without WASP. Each Flettner rotor is 30 meters tall and has a diameter of 5 m. Each Flettner rotor also has a top plate which is included in our modelling. The locations of these rotors relative to the aft perpendicular (AP) and fore perpendicular (FP) are depicted in Fig. 7.

Table 3
Summary of the studied route.

Leg #	Start	End	Voyage time (h)	Average speed (Kn)	Harbor time (h)
1	Oulu	Kemi	9	6.6	8
2	Kemi	Husum	17	13.0	6
3	Husum	Lübeck	52	13.9	6
4	Lübeck	Oulu	63	14.1	8

In this study, we analyse the current route and timetable of the existing diesel-powered Tavastland ship to simulate the operation of zero-emission vessels. The simulation covers a one-year period; weather and sea data for 2017 are incorporated into the simulations. The ship follows a weekly schedule, starting its voyages from Oulu (Finland) on Mondays at 21:00 CET and returning to the same port on the following Monday at 13:00 CET. Stops along the voyage include Kemi (Finland) on Tuesdays from 05:00 CET to 13:00 CET, Husum (Sweden) on Wednesdays from 06:00 CET to 12:00 CET, and Lübeck (Germany) on Fridays from 16:00 CET to 22:00 CET. Table 3 provides a summary of the information for the legs in the route, also shown in Fig. 8.

4. Results

The results in this paper are divided into two sections. In the first section, the power and energy requirements for the studied ship are determined. The effects of changing speed and the non-propulsive load on the required power and energy are also investigated in this section. In the second section, zero-emission propulsion systems are evaluated by assuming different charging scenarios and whether the Flettner rotors or fuel cell system are included in the propulsion system.

4.1. Determining power and energy requirements

Fig. 9(a) shows the total energy required to complete each voyage according to the schedule for the ship, both with and without WASP technology. As can be seen in the figure, the ship without WASP technology requires 1056.7 MWh at its peak, whereas the ship with WASP technology requires 673.4 MWh at its peak; this represents a decrease of approximately 35% in the maximum required energy when WASP technology is used. Figs. 9(c) and 9(b) show the required power at the way-points for the two ships. The values in these figures are

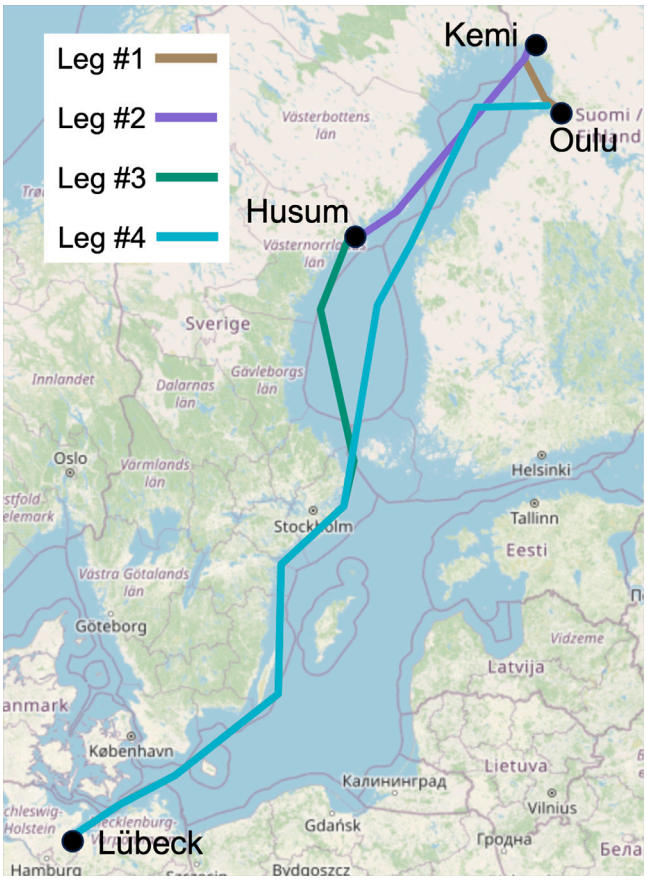

Fig. 8. The routes and legs considered in this study that define the voyage.

normalised by the maximum required power throughout the entire year. The maximum required power for the ship without WASP is 17.0 MW, while the maximum required power for the ship with WASP technology is only 12.3 MW, indicating a 27.6% reduction when WASP technology is employed. Additionally, the ship with WASP technology exhibits higher fluctuations in local required power relative to the maximum required power when compared to the ship without WASP technology. This increased fluctuation can be attributed to the ship's local power requirements being strongly influenced by wind conditions, as the thrust generated by the Flettner rotor significantly depends on these conditions. In contrast, the ship without WASP technology experiences much less dependency on wind conditions.

To investigate the impact of reducing speed on the maximum required power and maximum required energy, Fig. 10 shows the variation in these two parameters as a function of the speed reduction factor, which is defined as the ratio of the speed reduction to the average speed, as shown in the schedule shown in Table 3. The maximum required power generally decreases as the speed is reduced, but occasional spikes can be observed in these trends. These spikes occur due to changes in the ship's speed, which may occasionally lead to the ship travelling in harsher weather conditions, resulting in higher power demands. The results also indicate that, by reducing the speed, the maximum required power decreases to nearly 2 MW, which is the non-propulsive load of the ship. As for the maximum required energy, the general trend initially shows a decrease in energy demand when the speed is reduced, followed by an increase. This behaviour is a result of two competing effects. Initially, reducing the speed lowers the required power, as previously discussed; however, this also increases the duration of the voyage. Since energy is calculated as power multiplied by time, these competing effects contribute to the observed trend. It can be also seen that the effect of reducing the speed is more significant for the ship without WASP compared to the ship with WASP.

Fig. 11 shows the average required energy at different speed reduction factors compared to the average required energy at zero speed reduction factor for ships with varying non-propulsive loads. It can be observed that for both ships, the reduction in required energy strongly depends on the level of non-propulsive loads. For a ship with a non-propulsive load of 2 MW, the required energy can be reduced by 10% and 20% for ships with and without WASP, respectively. If the non-propulsive power is reduced to 500 kW, ships with and without WASP can reduce the required energy by 40% and 50%, respectively.

4.2. Designing zero-emission propulsion systems

In this subsection, we assess various zero-emission propulsion systems based on the power and energy requirements determined in the preceding subsection. The emphasis of this assessment is the practical and operational aspects of each system, while a cost analysis is beyond the scope of this study. Initially, we evaluate a zero-emission propulsion system which relies solely on a battery system as its energy source; subsequently, we explore a hybrid system incorporating both a battery system and a fuel cell system as part of the propulsion system.

4.2.1. Battery-driven system

To assess the practical implications of a battery-driven propulsion system, we evaluate two operational scenarios. In the first scenario, we assume that there is only one charging station located at the origin port of Oulu. In the second scenario, we assume that there is a second charging station with a power of 30 MW at the mid-port in Lübeck.

Scenario 1: only one charging station at the origin port

To determine the size of this battery system for this scenario, our initial assumption is that the ship must successfully complete all voyages according to the schedule, meaning that the battery system should provide for the maximum required energy shown in Fig. 9(a). For the ship with and without WASP, the maximum energy required is 673.9 MWh and 1056.5 MWh, respectively. Assuming that the battery's state of charge must be maintained between 20% and 80% to increase the lifetime of the battery and for safety, the required size of the battery system for the ship with and without WASP is 1123.2 MWh and 1761.0 MWh, respectively. Considering the weight of these batteries and the deadweight of the ship, the battery for the ship with WASP technology would be 64% of the deadweight and the battery for the ship without WASP would be 100.4% of the deadweight. Figs. 12(a) and 12(b) show the state of charge of the battery system at the way-points for the ships equipped with these assessed batteries. It can be seen that the state of charge of the battery at the end of the voyage is not always 20% due to the variation in the required energy for different voyages. Fig. 12(c) also illustrates the required charging rate needed at Oulu to charge the battery at the beginning of each voyage. It is evident that to ensure that the battery can be sufficiently charged for all voyages, charging rates of 84 MW and 128 MW are required for the ship with and without WASP, respectively.

The results indicate that, given the constraint that the ship must complete all voyages based on the schedule, the estimated size of the battery becomes excessively large, potentially constraining cargo space. To address this, we explore the possibility of accepting delays in the ship's schedule for some voyages and examine how this modified design constraint impacts the size of the battery system. Fig. 13(a) illustrates the delays for both the ship with and without WASP when the size of the battery system is reduced compared to the size of the battery system designed to strictly adhere to the schedule. Some voyages in this figure are labelled as cancelled, indicating that the battery system is unable to provide the required energy even with the acceptance of delays. The results indicate that by reducing the size of the battery system by 10%, the maximum delay for the ship with WASP is between 5 to 15%,

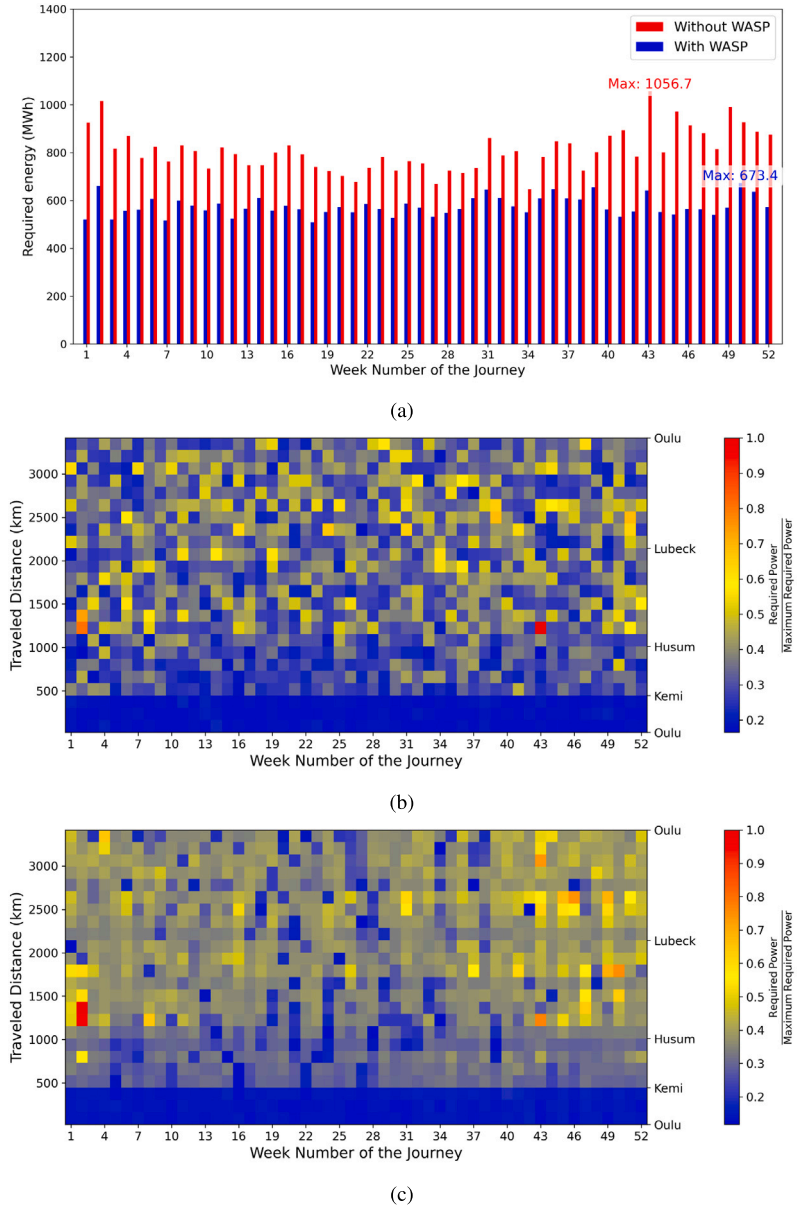

Fig. 9. The required energy and power to complete each voyage according to the schedule for 2017 for the ship with and without WASP: (a) the required energy to complete the voyage based on the schedule, (b) the power at the way-points normalised by the maximum required power (12.3 MW) for the ship with WASP technology, and (c) the required power at the way-points normalised by the maximum required power (17.0 MW) at the way-points for the ship without WASP.

occurring in two voyages. For the ship without WASP, a delay between 5 to 10% is predicted in one voyage in this case. A further 10% decrease in the size of the battery results in delays exceeding 20% for both ships; however, no cancelled trips are predicted. Further decreasing the size of the battery leads to expected cancelled voyages for both ships. Based on these findings, the weight of the required battery system for the ship with and without WASP is 51% and 80% of the deadweight, respectively, if delays are accepted for some voyages. This indicates a 20% reduction in battery weight compared to the requirement for completing all voyages.

Scenario 2: two charging stations at the origin and mid-ports

In this scenario, we assume a charging station exists with a maximum power of 30 MW at Lübeck port, just before the longest leg, in addition to the charging station at the origin port. To determine the required size of the battery system in this scenario, Fig. 14 shows the resulting delays and cancelled voyages when various battery system sizes are used in the propulsion system. It can be seen in the figure that if no delays are acceptable, the required battery system size for the ship with WASP is 786.8 MWh, with a weight that would account for 44% of the deadweight. Under the same condition for the ship without WASP, the required battery system size and deadweight contribution would be 1408.8 MWh and 80%, respectively. Alternatively, if delays are acceptable for certain voyages with the constraint that no voyage can be cancelled, the weight of the battery system can be further reduced to 32% of the deadweight for the ship with WASP and to 60% of the deadweight for the ship without WASP.

Table 4 provides a summary of the weight and size of the battery system considering different charging scenarios, whether delays are acceptable, and for ships with and without WASP technology. Our results indicate that utilising WASP technology can reduce the battery size by 30 to 40% in all scenarios, emphasising the significance of incorporating WASP technologies in zero-emission propulsion systems. This would enhance the feasibility of zero-emission propulsion systems by freeing up cargo space. Furthermore, it can be seen that, considering two charging stations and WASP technology while accepting

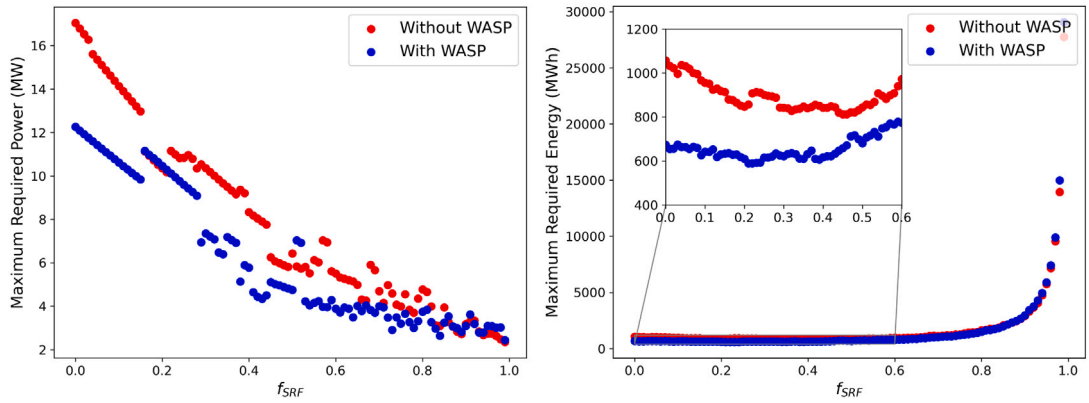

(a) (b)

Fig. 10. The average required energy to complete the voyage and the maximum required power at the way-points as a function of speed reduction factor (the ratio of the speed reduction to the average speed).

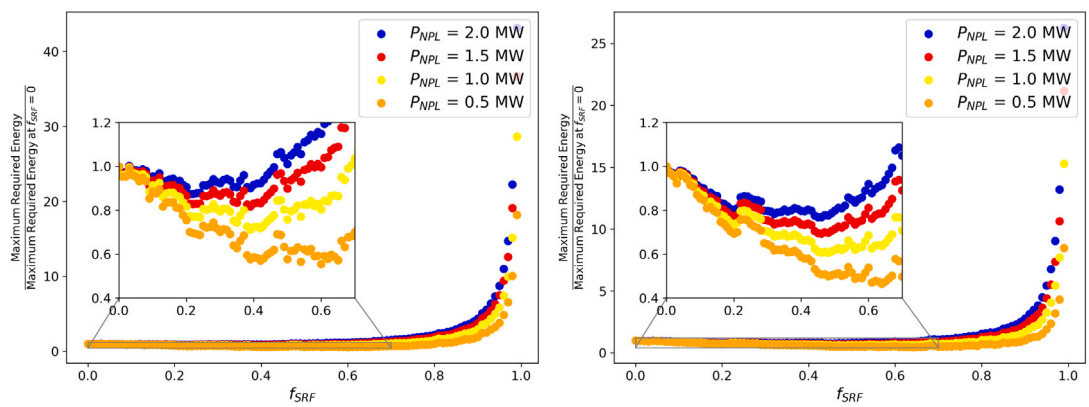

(a) (b)

Fig. 11. The maximum required energy over the maximum required energy at zero speed reduction factor as a function of speed reduction factor in the ships with different non-propulsive load, P_{NPL}: (a) ship with WASP technology, and (b) ship without WASP technology.

Table 4
Size, weight, and volume of the battery system in a battery-driven propulsion system considering different charging and operational scenarios.

Ships	Charging scenarios	Accepting delays	Size of the battery system (MWh)	Weight of the battery system (% DWT)	Volume of the battery system (m^3)
With WASP	Charging station at Oulu	No	1124.2	64	8647.7
		Yes	899.2	51	6916.9
	Charging stations at Oulu and Lübeck	No	786.6	44	6050.8
		Yes	576.2	32	4432.3
Without WASP	Charging station at Oulu	No	1761.0	100	13 546.2
		Yes	1408.8	80	10 836.9
	Charging stations at Oulu and Lübeck	No	1408.8	80	10 836.9
		Yes	1056.6	60	8127.7

delays in some voyages, even the smallest battery system accounts for approximately 32% of the deadweight. This implies that if the existing diesel-powered ship were to be retrofitted with a battery-driven propulsion system, a substantial portion of the cargo space would need to be used to house batteries, as the oil fuel would occupy only 8% of the deadweight in the existing diesel-powered ship. This suggests that, for the studied ship, exploring hybrid systems in which the battery system is integrated with a system having higher energy density than batteries should be considered, as described in detail in the following subsection.

4.2.2. Hybrid system - a combination of battery and fuel cell systems

In this subsection, we analyse a hybrid system that integrates both a battery system and a fuel cell system to provide the required energy for

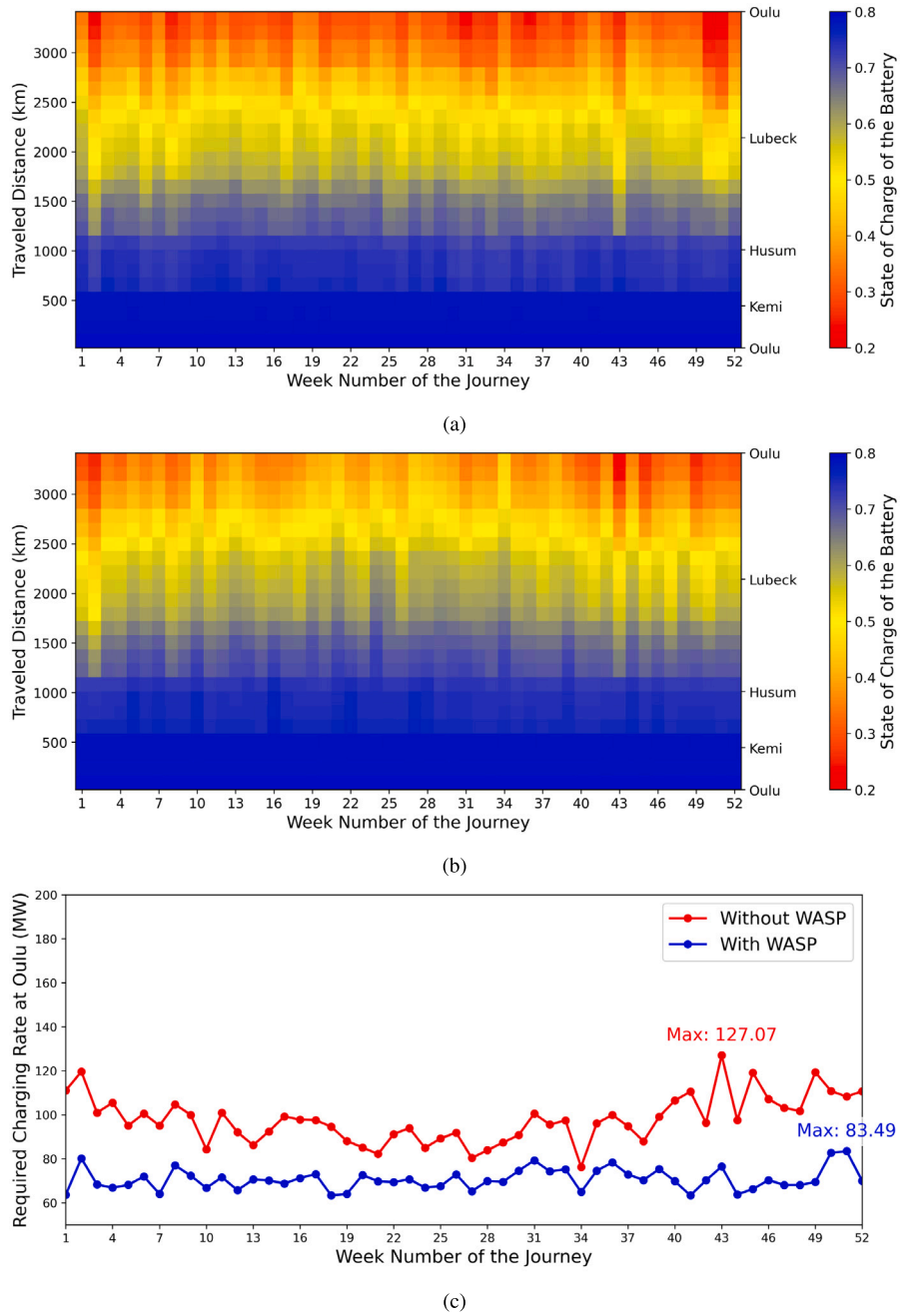

Fig. 12. The battery's state of charge at the ways points and the required charging rate at Oulu for the ships with and without WASP: (a) the battery's state of charge at the way-points for the ship with WASP, (b) the battery's state of charge at the way-points for the ship without WASP, and (c) the required charging rate at Oulu for the ship with and without WASP.

both propulsion systems and the constant load. We assume that the fuel cell system can deliver 2 MW, equivalent to the ship's constant load. Additionally, we consider two charging stations—one at the origin port, Oulu, and the second at the mid-port, Lübeck. The charging station at Lübeck has a maximum power of 30 MW. To determine the necessary size of the battery system in this scenario, Fig. 15 illustrates delays and cancelled voyages for ships with and without WASP, considering various battery sizes. These analyses assume the fuel cell operates at 100% load throughout all voyages. It is evident from this configuration that the battery size for ships with WASP can be reduced to 19% of the deadweight without causing any delays, and that the battery size can be reduced to 6% of the deadweight if delays are allowed. In this case, delays of more than 20% of the voyage time are expected for most voyages. For ships without WASP, a battery size with a weight of 50% of the deadweight is sufficient to complete all voyages without any delays. If delays are acceptable, the weight of the battery system can be reduced to 20% of the deadweight.

In addition to the weight of the battery systems, the weight of the fuel cell and the required hydrogen are also considered. The weight of the 2 MW fuel cell system is estimated to be 10 tonnes using the linear scaling presented in Section 2.1.2, which is less than 0.1% of the deadweight. Fig. 16 shows the weight of hydrogen consumed by the fuel cell system in all voyages for different ships and different sizes of the battery systems, considering cases for which delays are either allowed or not allowed. It can be seen from the figure that for the ship with and without WASP, 17.4 tonnes of hydrogen is consumed if the battery system is sized so that no delays are allowed, which is approximately 0.1% of the deadweight. If we size the battery system so

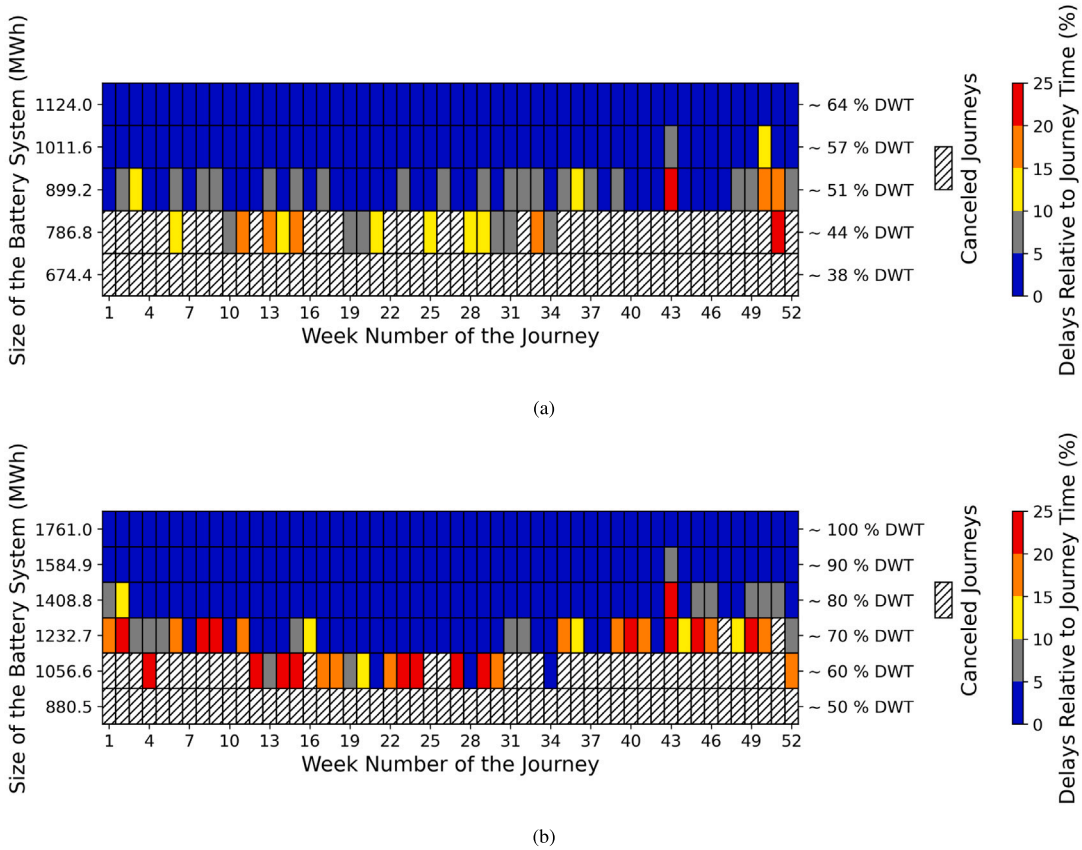

Fig. 13. Delays and cancelled voyages for the ship with and without WASP, for varying battery size: (a) ship with WASP, and (b) ship without WASP.

that delays are allowed, the maximum hydrogen consumed for the ship with WASP is 34.2 tonnes, while the value for the ship without WASP is 30.6 tonnes; these values are approximately 0.2% of the deadweight.

Table 5 provides a summary of the size and weight of the battery systems, fuel cell systems, and consumed hydrogen in the hybrid propulsion systems. A comparison of the total weight of the hybrid propulsion systems with the weight of the battery-driven system presented in Table 4 indicates that adding a 2 MW fuel cell would reduce the weight of the propulsion system by 20%–50% of the deadweight. Similar reduction can be seen in the volume occupied by the propulsion system. These reductions are due to the significantly higher specific energy and energy density of the fuel cell system compared to the battery system. Furthermore, considering the WASP technology and a hybrid system, the size and weight of the propulsion system would be 19.2% of the deadweight if no delays are accepted. This implies that replacing the existing diesel-powered propulsion system, which accounts for approximately 8% of the deadweight, would necessitate compromising only around 11% of the cargo space. The results also show that this reduction in cargo space can be minimised or eliminated if delays in some voyages are accepted.

Detail analysis of the operation of hybrid propulsion systems

Based on the results listed in Table 5, we examine the operation of two hybrid propulsion systems for the ships with and without WASP in greater detail. For both vessels, we assume the propulsion system comprises a 2 MW fuel cell system and a battery system, and a charging station with a capacity of 30 MW is available at the Lübeck port. The battery system sizes for ships with and without WASP are 337.2 MWh and 880.7 MWh, respectively. These sizes are determined to ensure that the combination of the fuel cell and battery system is sufficient to maintain the schedule throughout the entire year without any delays. Since there are two energy providers in the propulsion system, a strategy must be implemented in the energy management system to distribute power and energy between the fuel cell and battery systems. The simplest such strategy assumes that the fuel cell operates at 100% load to supply the constant non-propulsive load, while the battery system is responsible for providing the propulsive load. Using this strategy, Fig. 17 shows the state of charge of the battery system for the two ships. It is evident from the figure that, for both ships, the state of charge of the battery system is higher than 20% at the end of several voyages, indicating that there is excess energy remaining in the battery system. This surplus is a result of the propulsion system being designed to meet the maximum required energy for a voyage throughout the entire year which makes it larger than required for the voyages with less required energy. Due to the fuel cell system operating at 100% load, the battery system does not discharge to its minimum state of charge at the end of those voyages.

The simulation results are also utilised to estimate the size of the hydrogen tank and charging stations at the port. The amount of hydrogen used during a voyage for both ships is 17.4 tonnes, indicating that a tank of this size would be sufficient. The tank volume, employing LH2 and CcH2 technologies, is 245.1 and 217.5 m^3, respectively. The total amount of hydrogen consumed throughout the year for both ships is 904.9 tonnes. The required charging rate at the ports is depicted in Fig. 18. As can be seen in the figure, the maximum charging rate used at Lübeck is 30 MW, which is the assumed charging rate for both ships. The highest charging rates at Oulu for the ship, with and without WASP, are 26.4 and 64.9 MW, respectively.

The results shown in Fig. 17 indicate that assuming a constant load for the fuel cell system results in excess energy remaining in the battery

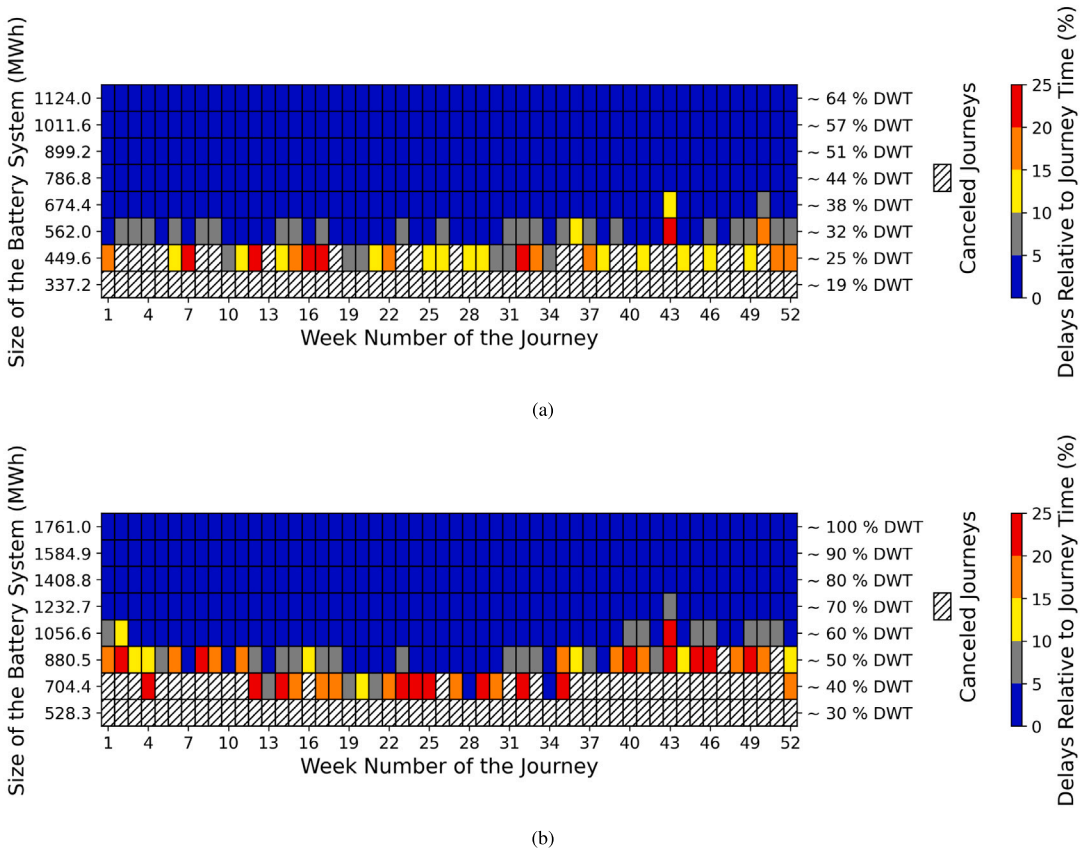

Fig. 14. Delays and cancelled voyages for the ship with and without WASP when a charging station with a power of 30 MW at Lübeck is assumed, for varying battery sizes: (a) ship with WASP, and (b) ship without WASP.

Table 5
Size, weight, and volume of the battery systems, fuel cell systems, and consumed hydrogen in a hybrid propulsion system considering different operational scenarios (The volume of hydrogen is reported based on two hydrogen storage technologies: liquid hydrogen (LH2) and cryo-compressed hydrogen (CCH2)).

Ships	Accepting delays	Size of the battery system (MWh)	Weight of the battery system (% DWT)	Volume of the battery system (m^3)	Size of the fuel cell system (MW)	Weight of the fuel cell system (% DWT)	Volume of the fuel cell system (m^3)	Weight of the used hydrogen (% DWT)	Volume of the used hydrogen (m^3)
With WASP	No	337.2	19	2593.8	2	0.1	19.7	0.1	245.1 (LH2) 217.5 (CCH2)
	Yes	112.4	6	864.6	2	0.1	19.7	0.2	481.7 (LH2) 427.5 (CCH2)
Without WASP	No	880.5	50	6773.1	2	0.1	19.7	0.1	245.1 (LH2) 217.5 (CCH2)
	Yes	352.2	20	2709.2	2	0.1	19.7	0.2	431.0 (LH2) 382.5 (CCH2)

system at the end of certain voyages. This surplus energy can be used to reduce the load on the fuel cell, thereby reducing the consumption of hydrogen. To quantify the potential reduction in hydrogen consumption, we determine the fuel cell loads at the way-points to minimise the hydrogen consumption. The optimisation problem to determine these loads can be defined as:

$$\min\ OF(Z_{fc,i}) = M_{H_2} + 1000 * \max(Err_{PI,i}) \tag{31}$$

where $Z_{fc,i}$ is the fuel cell load at the way-points, M_{H_2} is the mass of consumed hydrogen over the entire voyage, and $Err_{PI,i}$ is the relative power imbalance error at the way-points. Note that the presence of $\max(Err_{PI,i})$ with the weighting factor of 1000 is to ensure that the relative power imbalance error is minimised first. This optimisation problem is solved using sequential least squares programming (SLSQP) for all the voyages throughout the year. The optimisation continues until the maximum relative power imbalance error is less than 0.001.

Fig. 19 shows the battery system's state of charge using the optimised fuel cell loads for both ships. It can be observed that, in contrast to the scenario in which the fuel cell operates at 100% load continuously, shown in Fig. 17, the state of charge for the battery system is consistently near 20% by the end of voyage. For the ship with WASP, the battery is depleted before reaching Lübeck port and subsequently recharged to 80% state of charge at the port using the available 30 MW charging power. Conversely, for the ship without WASP, the state of charge reaches around 30% just before Lübeck, and the charging at Lübeck manages to increase the battery's state of charge

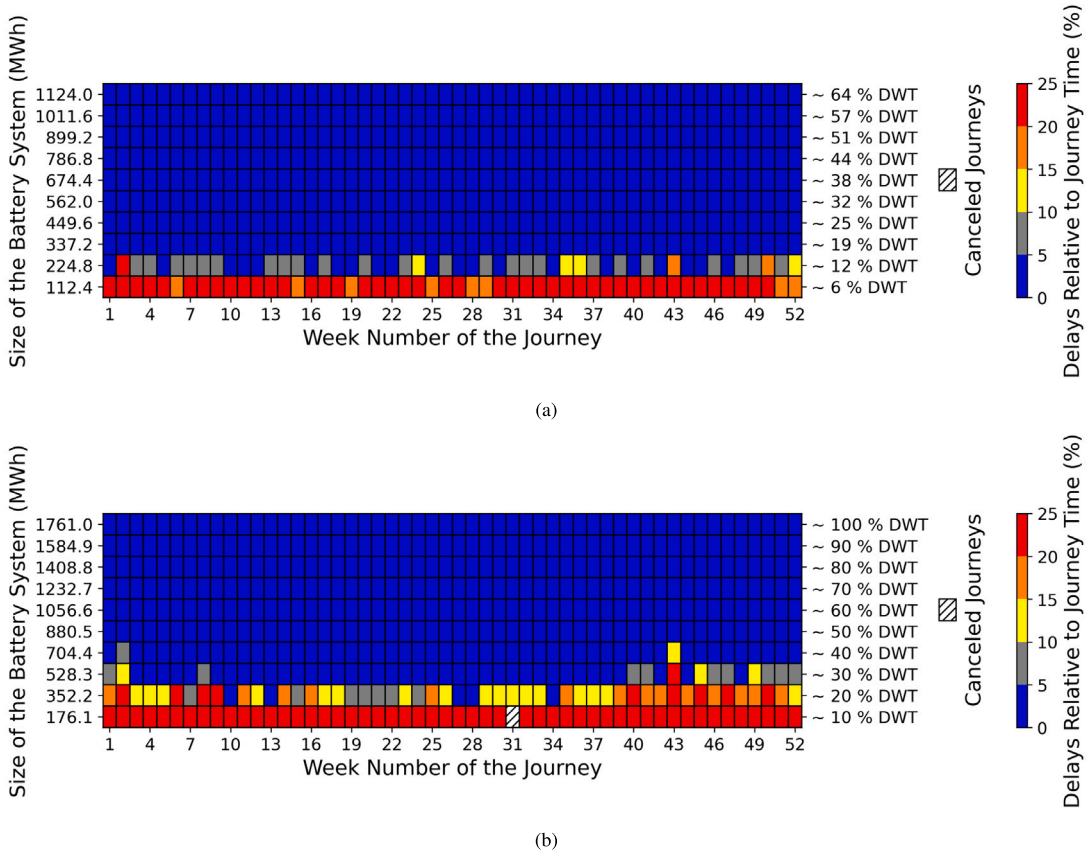

Fig. 15. Delays and cancelled voyages for the ship with and without WASP considering different battery sizes, a charging station of 30 MW, and a 2 MW fuel cell system: (a) ship with WASP, and (b) ship without WASP.

to around 60%. The difference between the two ships relates to the size of the battery systems; the ship with WASP has a smaller battery system compared to the ship without WASP.

Fig. 20 shows the optimised fuel cell loads for both ships. It can be seen that while the variation during each voyage is minimal, the voyage-to-voyage variation is significant. This variation is much higher for the ship without WASP compared to the ship with WASP. The reason for this is that the combination of assumed battery and fuel cell systems is determined so that it is sufficient to meet the maximum required energy, and this combination has excess capacity for the voyages for which the required energy is lower. For the ship without WASP, the large variation in required energy throughout the year allows the battery system alone to provide energy for some voyages. This results in the fuel cell operating on zero load, as depicted in Fig. 20(b). In contrast, for the ship with WASP, the maximum required energy is near the average required energy for all voyages. For most voyages, this implies that the fuel cell should operate at relatively high loads to meet the energy demand.

Figs. 21(a) and 21(b) show the mass of consumed hydrogen throughout the voyages. The maximum consumption of hydrogen is 17.8 and 17.3 tonnes for the ship with and without WASP, respectively. This level of consumed hydrogen is very close to the value when the fuel cell is running on 100% load, meaning that the size of the hydrogen tank would not change. It can be also seen that the variation of the consumed hydrogen is higher in the ship without WASP, which is the result of large variations in the fuel cell load, as shown in Fig. 20(b). The amount consumed hydrogen over the entire year for the ship with and without WASP is 596.4 and 229.5 tonnes, respectively, which is a reduction of 35 and 75% of the consumed hydrogen compared to 100% load fuel cell conditions. Figs. 21(c) and 21(d) show the required charging rate at the Oulu and Lübeck ports for the two ships. It can be seen that the charging rate at Lubeck is nearly 30 MW which is close to the assumed charging rate. It can be also seen that for the ship without WASP, the charging rate needed at Oulu has a maximum of approximately 26 MW, while for the ship without WASP, the maximum charging rate is around 66 MW. This is very close to the case in which the fuel cell is operating at 100% load.

5. Conclusions

In this study, we investigate hybrid battery-hydrogen-wind powered propulsion systems offering the potential for zero emissions for a benchmark merchant ship operating in the Baltic Sea. The study includes two ship variants: one integrated with WASP, featuring four Flettner rotors, and the other without WASP. The investigations are performed using an in-house built platform capable of simulating ships with different zero-emission propulsion systems and their long-term operations. Employing the models described in this paper, we determine the power and energy requirements for both ships travelling along a predefined route based on a realistic one-year schedule. The analysis shows that by incorporating WASP technology, a substantial reduction of 35% in required energy and 28% in power can be achieved. Furthermore, our results reveal that, while reducing the ship's speed leads to a substantial decrease in the required power, the corresponding reduction in required energy is limited to 10%–15%, which can be directly attributed to the high non-propulsive load for the ship. Additionally, we demonstrate that by reducing the non-propulsive load from 2 MW to 500 kW, it is possible to reduce the energy demand by 40%–50% simply by decreasing the

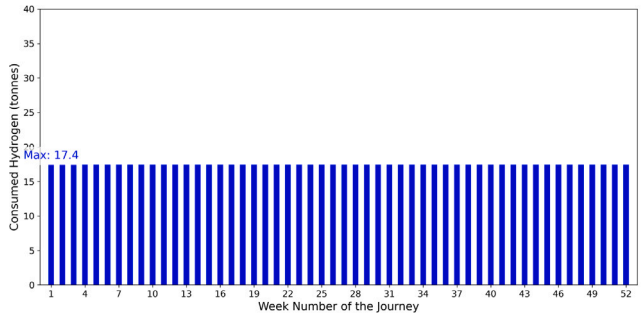

(a) Ship with WASP when no delays allowed

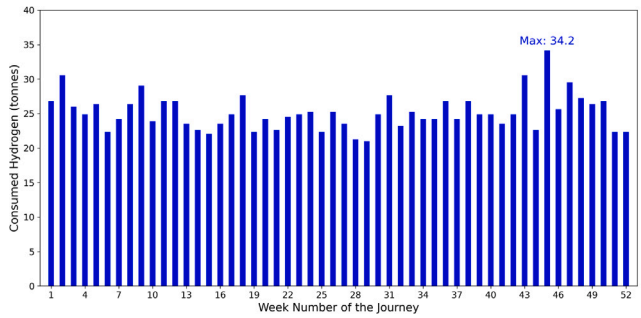

(b) Ship with WASP when delays are allowed

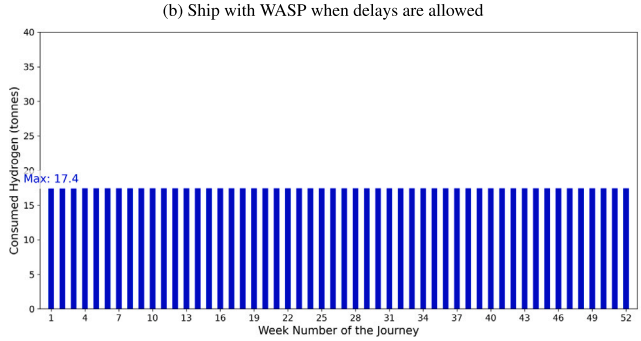

(c) Ship without WASP when no delays are allowed

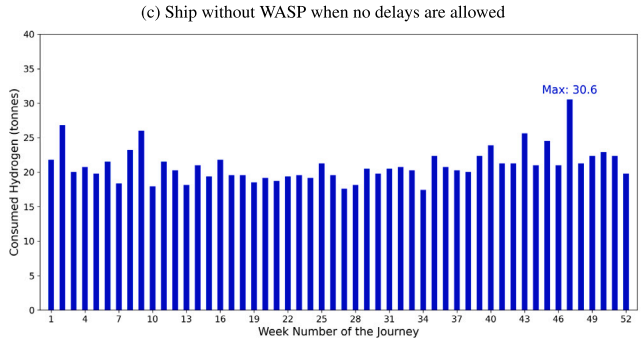

(d) Ship without WASP when delays are allowed

Fig. 16. The weight of hydrogen used by the fuel cell system for the ship with and without WASP considering whether delays are allowed or not.

ship's speed, highlighting the importance of increasing the efficiency of non-propulsive energy consumers on the ship.

Utilising the energy requirements over a one-year operational period, we initially investigate a zero-emission propulsion system including solely a battery system as the primary energy source. Two charging scenarios are considered: charging only at the origin port, and charging at the origin port as well as at a charging station at the mid-port. For each scenario, we assess whether delays from the defined schedule are permissible. The analysis reveals that, without incorporating WASP technology and with only one charging station at the origin port, a battery-driven propulsion system is impractical for the studied merchant ship because its weight is approximately 100% of the ship's deadweight. By integrating WASP technology and adding a charging station at the mid-port, the weight of the propulsion system decreases significantly, but still accounts for approximately 44% of the deadweight, necessitating compromises in cargo space. This indicates that for the zero-emission propulsion system to be feasible, the battery system should be hybridised with an energy source possessing higher specific energy. We explore such a system in which a battery system is integrated with a fuel cell system capable of producing 2 MW, equivalent to the non-propulsive load of the ship. In this case, the weight of the propulsion system can be reduced to 19.2% of the deadweight for the ship with WASP and 50.2% for the ship without WASP. We also examine two operational modes for this battery/fuel cell hybrid system. In the first operational mode, the fuel cell consistently operates at 100% load, while in the second, the fuel cell loads are optimised at the way-points to minimise hydrogen fuel consumption. The results indicate that optimising the fuel cell loads can lead to a 35% and 75% reduction in hydrogen consumption for the ship with and without WASP, respectively, for the entire year compared to conditions with a 100% load on the fuel cell. This highlights the importance of designing an energy management system to optimise the operation of the hybrid system.

The results in this paper show the feasibility of zero emission systems for a merchant vessel from a practical perspective. However, there are several challenges for implementing such a system which should be addressed in future research. While the operation of the proposed propulsion system is zero emission, it is crucial to evaluate the environmental impact of such a system using life cycle analysis, considering different scenarios for the production of electricity and hydrogen used in this propulsion system. Furthermore, cost analysis should evaluate the economic aspect of such a system. This entails considering operational costs such as electricity and hydrogen prices, as well as investment costs like battery and fuel cell systems. Additionally, upgrading ports for charging facilities and hydrogen bunkering should be evaluated.

CRediT authorship contribution statement

Mohammad Hossein Arabnejad: Writing – original draft, Validation, Software, Methodology, Investigation, Formal analysis, Data curation, Conceptualization. **Fabian Thies:** Writing – review & editing, Supervision, Software, Methodology, Investigation, Funding acquisition, Formal analysis, Conceptualization. **Hua-Dong Yao:** Writing – review & editing, Supervision, Funding acquisition, Conceptualization. **Jonas W. Ringsberg:** Writing – review & editing, Supervision, Funding acquisition, Conceptualization.

Declaration of competing interest

The authors declare that they have no known competing financial interests or personal relationships that could have appeared to influence the work reported in this paper.

Acknowledgements

This study received funding from Chalmers Transport Area of Advance and Chalmers University of Technology Foundation for the strategic research project "Hydro- and aerodynamics".

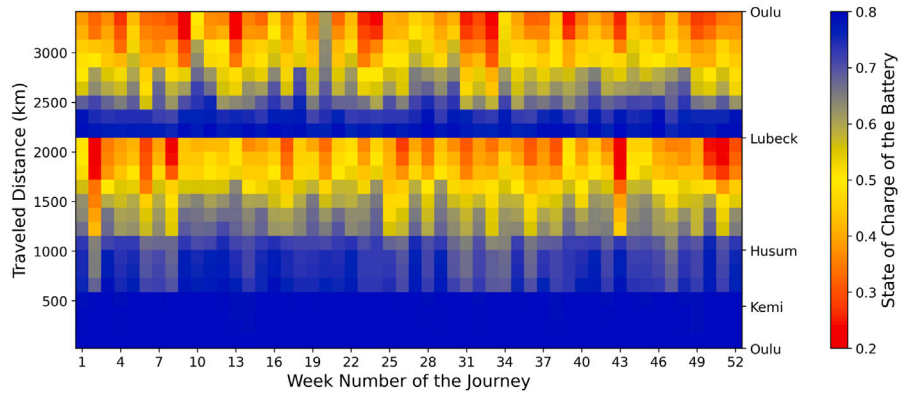

(a)

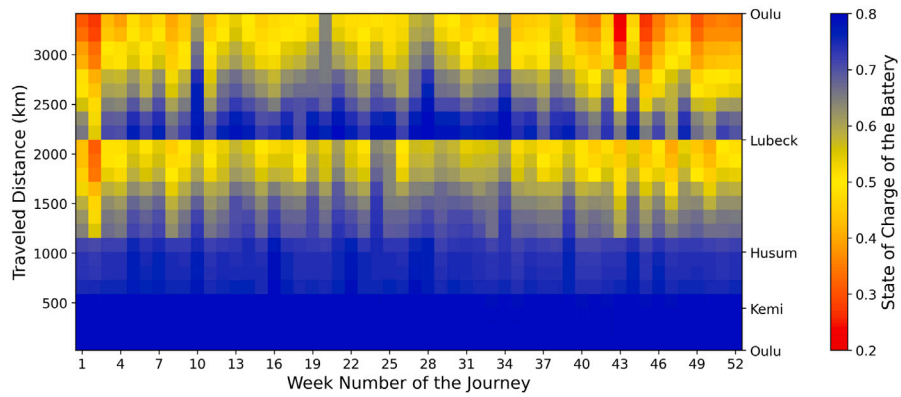

(b)

Fig. 17. The battery's state of charge at the way-points for hybrid fuel-cell-battery systems when the 2 MW fuel is always operating at full load: (a) ship with WASP, and (b) ship without WASP.

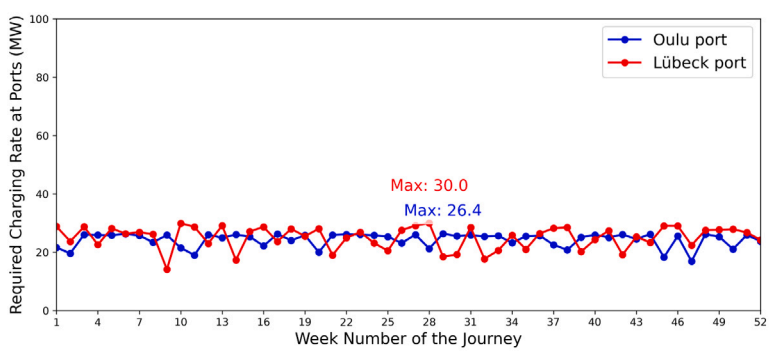

(a)

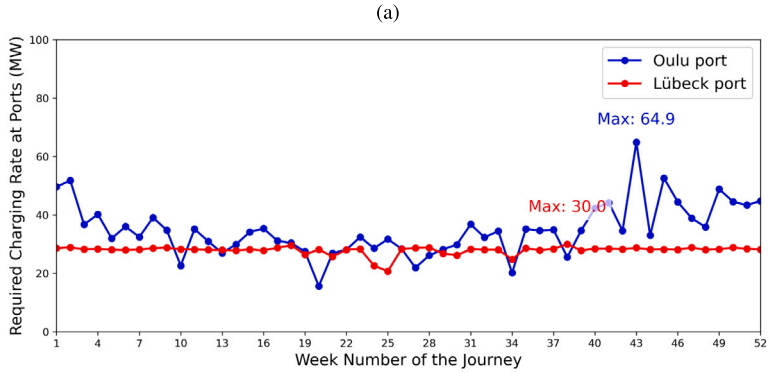

(b)

Fig. 18. The required charging rate at the ports for the hybrid fuel-cell-battery systems when the 2 MW fuel cell always operates at full load: (a) ship with WASP, and (b) ship without WASP.

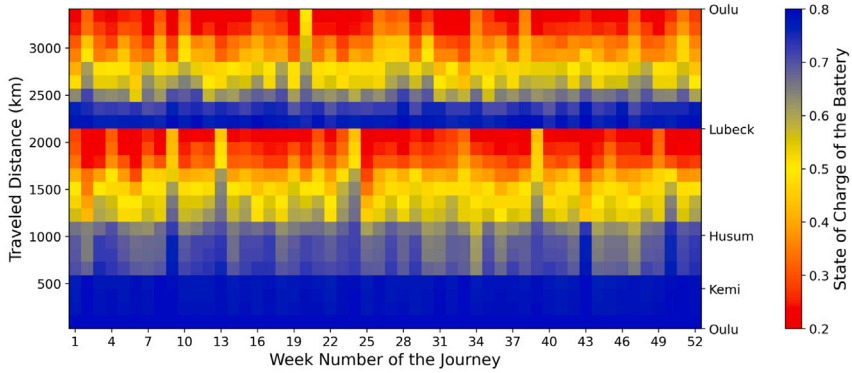

(a)

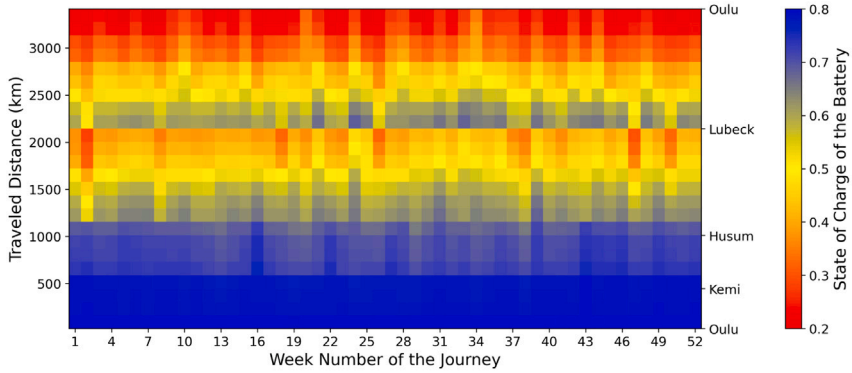

(b)

Fig. 19. State of charge of the battery systems using the optimised fuel cell loads in the optimisation problem of Eq. (31) for: (a) ship with WASP, and (b) ship without WASP.

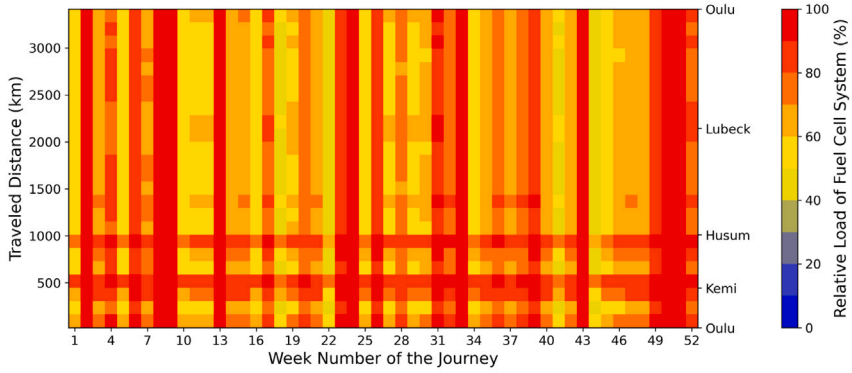

(a)

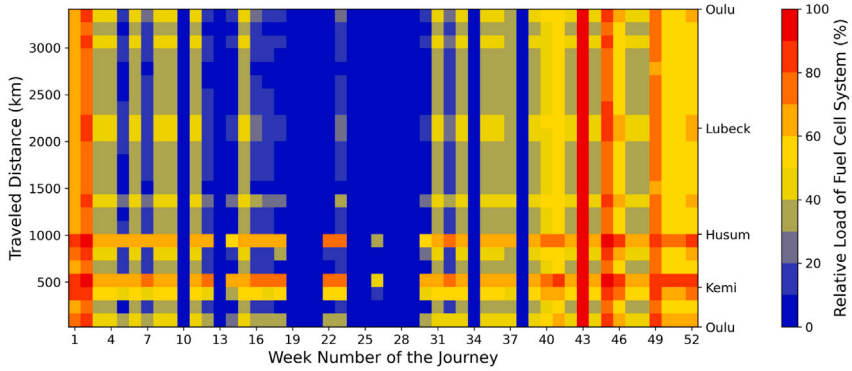

(b)

Fig. 20. The optimised fuel cell loads in the optimisation problem of Eq. (31) for: (a) ship with WASP, and (b) ship without WASP.

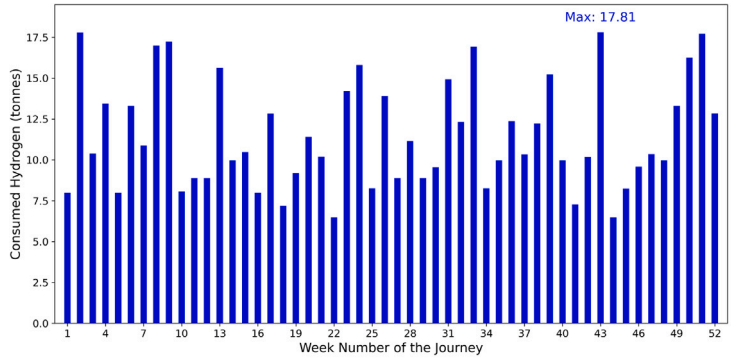

(a)

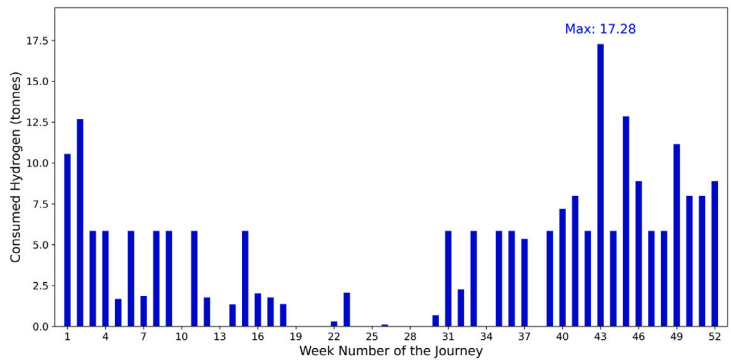

(b)

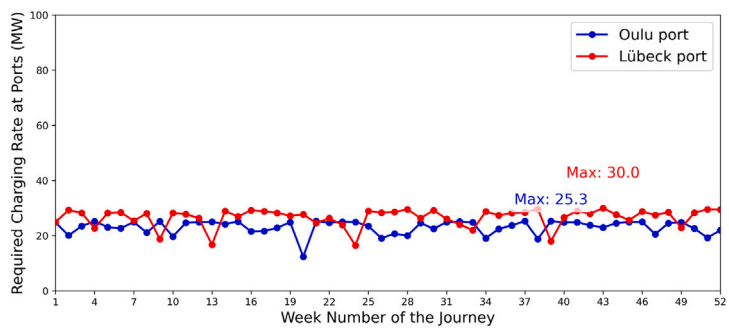

(c)

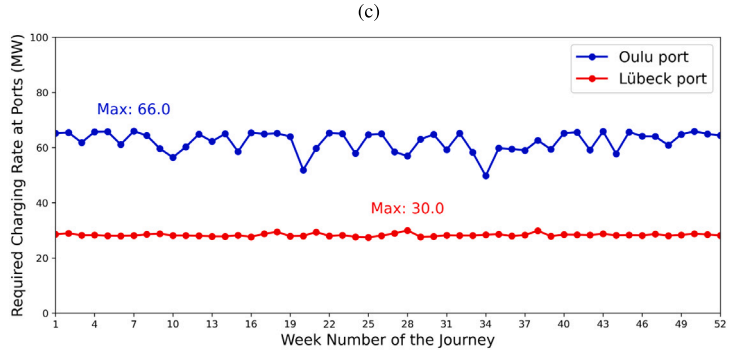

(d)

Fig. 21. Consumed hydrogen and the required charging rate at the ports using the optimised fuel cell loads in the optimisation problem of Eq. (31) for: (a) consumed hydrogen for the ship with WASP, and (b) consumed hydrogen for ship without WASP, (c) charging rate at the ports for the ship with WASP, (d) charging rate at the ports for the ship without WASP.

References

Abbasov, F., Earl, T., Ambel, C.C., Hemmings, B., Gilliam, L., 2018. Roadmap to decarbonising European shipping. Technical report, Hydrogen Knowledge Centre.

Alkhaledi, A.N., Sampath, S., Pilidis, P., 2023. Techno environmental assessment of flettner rotor as assistance propulsion system for LH2 tanker ship fuelled by hydrogen. Sustain. Energy Technol. Assess. 55, 102935.

Alnes, O., Eriksen, S., Vartdal, B.J., 2017. Battery-powered ships: A class society perspective. IEEE Electrif. Mag. 5 (3), 10–21.

Ammar, N.R., Seddiek, I.S., 2022. Wind assisted propulsion system onboard ships: Case study flettner rotors. Ships and Offshore Struct. 17 (7), 1616–1627.

Balestra, L., Schjølberg, I., 2021. Modelling and simulation of a zero-emission hybrid power plant for a domestic ferry. Int. J. Hydrog. Energy 46 (18), 10924–10938.

Brooks, M.R., Faust, P., 2018. 50 years of review of maritime transport, 1968–2018: Reflecting on the past, exploring the future. Technical report, UNCTAD.
Casey, M., Robinson, C., 2013. A method to estimate the performance map of a centrifugal compressor stage. J. Turbomach. 135 (2), 021034.
Corbo, P., Migliardini, F., Veneri, O., 2007. Experimental analysis and management issues of a hydrogen fuel cell system for stationary and mobile application. Energy Convers. Manag. 48 (8), 2365–2374.
Damian, S.E., Wong, L.A., Shareef, H., Ramachandaramurthy, V.K., Chan, C., Moh, T., Tiong, M.C., 2022. Review on the challenges of hybrid propulsion system in marine transport system. J. Energy Storage 56, 105983.
Du, W., Li, Y., Zhang, G., Wang, C., Zhu, B., Qiao, J., 2022. Energy saving method for ship weather routing optimization. Ocean Eng. 258, 111771.
Energy, C., 2023. Corvus blue whale. URL https://corvusenergy.com/products/energy-storage-solutions/corvus-blue-whale/. (Accessed: 13 July 2023).
Faber, J., et al., 2020. Fourth IMO GHG Study 2020. Technical report, International Maritime Organization.
Gagatsi, E., Estrup, T., Halatsis, A., 2016. Exploring the potentials of electrical waterborne transport in europe: the E-ferry concept. Transp. Res. Procedia 14, 1571–1580.
Han, J., Charpentier, J.F., Tang, T., 2012. State of the art of fuel cells for ship applications. In: 2012 IEEE International Symposium on Industrial Electronics. IEEE, pp. 1456–1461.
Harvald, S.A., 1992. Resistance and Propulsion of Ships. Wiley-Interscience.
Holtrop, J., Mennen, G., 1982. An approximate power prediction method. Int. Shipbuild. Progress 29 (335), 166–170.
International Maritime Organization, 2020. IMO 2020 – cutting sulphur oxide emissions. URL https://www.imo.org/en/MediaCentre/HotTopics/Pages/Sulphur-2020.aspx.
International Maritime Organization, 2023. 2023 IMO strategy on reduction of GHG emissions from ships. Technical report, Marine Environment Protection Committee, International Maritime Organization.
ITTC, 2021. Preparation, conduct, and analysis of speed/power trials. Technical report, International Towing Tank Conference.
Julià, E., Tillig, F., Ringsberg, J.W., 2020. Concept design and performance evaluation of a fossil-free operated cargo ship with unlimited range. Sustainability 12 (16), 6609.
Karimi, S., Zadeh, M., Suul, J.A., 2020. Shore charging for plug-in battery-powered ships: Power system architecture, infrastructure, and control. IEEE Electrif. Mag. 8 (3), 47–61.
Kersey, J., Popovich, N.D., Phadke, A.A., 2022. Rapid battery cost declines accelerate the prospects of all-electric interregional container shipping. Nat. Energy 7 (7), 664–674.
Kramer, J.A., Steen, S., Savio, L., 2016. Drift forces—wingsails vs. Flettner rotors. In: Proceedings of the International Conference on High Performance Marine Vehicles. Cortona, Italy, pp. 17–19.
Kristensen, H., Lützen, M., 2012. Prediction of resistance and propulsion power of ships. Clean Shipping Curr. 1 (6), 1–52.
Letafat, A., Rafiei, M., Sheikh, M., Afshari-Igder, M., Banaei, M., Boudjadar, J., Khooban, M.H., 2020. Simultaneous energy management and optimal components sizing of a zero-emission ferry boat. J. Energy Storage 28, 101215.
Li, D., Leer-Andersen, M., Allenström, B., 2012. Performance and vortex formation of flettner rotors at high Reynolds numbers. In: 29th Symposium on Naval Hydrodynamic. Gothenburg.
Lindstad, H., Asbjørnslett, B.E., Strømman, A.H., 2011. Reductions in greenhouse gas emissions and cost by shipping at lower speeds. Energy Policy 39 (6), 3456–3464.
Lindstad, E., Stokke, T., Alteskjær, A., Borgen, H., Sandaas, I., 2022. Ship of the future–a slender dry-bulker with wind assisted propulsion. Maritime Transp. Res. 3, 100055.
Liu, S., Papanikolaou, A., 2020. Regression analysis of experimental data for added resistance in waves of arbitrary heading and development of a semi-empirical formula. Ocean Eng. 206, 107357.
Lu, R., Ringsberg, J.W., 2020. Ship energy performance study of three wind-assisted ship propulsion technologies including a parametric study of the flettner rotor technology. Ships Offshore Struct. 15 (3), 249–258.
Madsen, R., Klebanoff, L., Caughlan, S., Pratt, J., Leach, T., Appelgate Jr., T., Kelety, S., Wintervoll, H.-C., Haugom, G., Teo, A., Gosh, S., 2020. Feasibility of the zero-v: A zero-emissions hydrogen fuel-cell coastal research vessel. Int. J. Hydrog. Energy 45 (46), 25328–25343.
Oosterveld, M., van Oossanen, P., 1975. Further computer-analyzed data of the wageningen B-screw series. Int. Shipbuild. Progr. 22 (251), 251–262.
Perčić, M., Frković, L., Pukšec, T., Ćosić, B., Li, O.L., Vladimir, N., 2022. Life-cycle assessment and life-cycle cost assessment of power batteries for all-electric vessels for short-sea navigation. Energy 251, 123895.
Plett, G., 2015. Battery management systems, Volume I: Battery modeling, vol. 1, Artech House.
Pukrushpan, J., 2003. Modeling and control of fuel cell systems and fuel processors (Ph.D. thesis). University of Michigan.
Schneekluth, H., Bertram, V., 1998. Ship design for efficiency and economy. vol. 218, Butterworth-Heinemann Oxford.
Sofiev, M., Winebrake, J.J., Johansson, L., Carr, E.W., Prank, M., Soares, J., Vira, J., Kouznetsov, R., Jalkanen, J., Corbett, J.J., 2018. Cleaner fuels for ships provide public health benefits with climate tradeoffs. Nat. Commun. 9 (1), 406.
Thies, F., Ringsberg, J.W., 2023. Wind-assisted, electric, and pure wind propulsion–the path towards zero-emission RoRo ships. Ships Offshore Struct. 18 (8), 1229–1236.
Tillig, F., 2020. Simulation model of a ship's energy performance and transportation costs. Chalmers Tekniska Hogskola (Sweden).
Tillig, F., Ringsberg, J., 2020. Design, operation and analysis of wind-assisted cargo ships. Ocean Eng. 211, 107603.
Tillig, F., Ringsberg, J., Mao, W., Ramne, B., 2017. A generic energy systems model for efficient ship design and operation. Proc. Instit. Mech. Eng. M 231 (2), 649–666.
Wan, Y., Guan, J., Xu, S., 2017. Improved empirical parameters design method for centrifugal compressor in PEM fuel cell vehicle application. Int. J. Hydrogen Energy 42 (8), 5590–5605.
Wang, Z., Dong, B., Wang, Y., Li, M., Liu, H., Han, F., 2023. Analysis and evaluation of fuel cell technologies for sustainable ship power: Energy efficiency and environmental impact. Energy Convers. Manag. X 100482.
Wang, H., Mao, W., Eriksson, L., 2019. A three-dimensional dijkstra's algorithm for multi-objective ship voyage optimization. Ocean Eng. 186, 106131.
Wang, Z., Wang, Y., Afshan, S., Hjalmarsson, J., 2021. A review of metallic tanks for H2 storage with a view to application in future green shipping. Int. J. Hydrog. Energy 46 (9), 6151–6179.
Xing, H., Spence, S., Chen, H., 2020. A comprehensive review on countermeasures for CO2 emissions from ships. Renew. Sustain. Energy Rev. 134, 110222.
Xing, H., Stuart, C., Spence, S., Chen, H., 2021a. Alternative fuel options for low carbon maritime transportation: Pathways to 2050. J. Clean. Prod. 297, 126651.
Xing, H., Stuart, C., Spence, S., Chen, H., 2021b. Fuel cell power systems for maritime applications: Progress and perspectives. Sustainability 13 (3), 1213.
Zheng, F., Xing, Y., Jiang, J., Sun, B., Kim, J., Pecht, M., 2016. Influence of different open circuit voltage tests on state of charge online estimation for lithium-ion batteries. Appl. Energy 183, 513–525.
Zhou, M., Yang, M., Wu, X., 2019. Research on control strategy of quasi-z source network DC/DC converter for fuel cell vehicle. DEStech Trans. Environ. Energy Earth Sci..